J. Fluid Mech. (2021), *vol*. 910, A4. © The Author(s), 2021.
Published by Cambridge University Press
doi:10.1017/jfm.2020.915

Effect of actuation method on hydrodynamics of elastic plates oscillating at resonance

Ersan Demirer[1], **Yu-Cheng Wang**[1], **Alper Erturk**[1] **and Alexander Alexeev**[1],†

[1]George W. Woodruff School of Mechanical Engineering, Georgia Institute of Technology, Atlanta, GA 30332, USA

(Received 6 April 2020; revised 3 August 2020; accepted 15 October 2020)

In this work we investigate the effects of two distinct actuation methods on the hydrodynamics of elastic rectangular plates oscillating at resonance. Plates are driven by plunging motion at the root or actuated by a distributed internal bending moment at Reynolds numbers between 500 and 4000. The latter actuation method represents internally actuated smart materials and emulates the natural ability of swimming animals to continuously change their shapes with muscles. We conduct experiments with plunging elastic plates and piezoelectric plate actuators that are simulated using a fully coupled three-dimensional computational model based on the lattice Boltzmann method. After experimental validation the computational model is employed to probe plate hydrodynamics for a wide range of parameters, including large oscillation amplitudes which prompts nonlinear effects. The comparison between the two actuation methods reveals that, for the same level of tip deflection, externally actuated plates significantly outperform internally actuated plates in terms of thrust production and hydrodynamic efficiency. The reduced performance of internally actuated plates is associated with their suboptimal bending shapes which leads to a trailing edge geometry with enhanced vorticity generation and viscous dissipation. Furthermore, the difference in actuation methods impacts the inertia coefficient characterizing the plate oscillations, especially for large amplitudes. It is found that the inertia coefficient strongly depends on the tip deflection amplitude and the Reynolds number, and actuation method, especially for larger amplitudes.

Key words: flow–structure interactions, swimming/flying, propulsion

1. Introduction

Among different fluid–structure interaction problems, the problem of the unsteady hydrodynamics of an elastic plate oscillating under water has been under the scrutiny of numerous researchers due to its fundamental aspects and diverse practical applications (Sfakiotakis, Lane & Davies 1999; Dowell & Hall 2001; Amabili & Paidoussis 2003; Chen *et al.* 2006; Shelley & Zhang 2011; Hou, Wang & Layton 2012). The challenging physics in this problem arises from the dynamic coupling between the elastic deformation of the plate and the unsteady fluid motion. As an elastic plate oscillates in a fluid, it bends due to its own inertia, elastic forces and hydrodynamic forces, yielding complex dynamic

† Email address for correspondence: alexander.alexeev@me.gatech.edu

shape changes. The plate dynamics, in turn, imposes the motion on the viscous fluid surrounding the plate. Thus, the coupling between the plate dynamic deformation and the unsteady hydrodynamic loading needs to be resolved to understand the plate motion and to rationalize the resulting hydrodynamic forces associated with complex three-dimensional flow structures generated by the oscillating plate.

Most biological systems involved in flying or swimming consist of deformable surfaces actuated with muscle contractions and passive deformation due to the surrounding flow (Fish & Lauder 2006). In the case of swimming, fish are able to achieve swimming velocities, maximum burst speeds and efficiencies far exceeding the best man-made designs of comparable size (Scaradozzi *et al.* 2017). Elasticity is often used by animals to generate complex deformation patterns using simple actuation (Jayne & Lauder 1995; McHenry, Pell & Long 1995; Lauder & Tytell 2005). Multiple studies explored the movement of fish fins that undergo complex and inherently three-dimensional motion (Flammang & Lauder 2009; Esposito *et al.* 2012; Lauder & Tangorra 2015). Through this complex motion and local change in elasticity, fish can achieve efficient swimming and manoeuvring.

Small and medium size fish measure up to 10–20 cm and reach swimming velocities up to several body lengths per second leading to Reynolds number $Re \sim 10^2$–10^5. In this range of Reynolds number both inertial and viscous effects play a substantial role in the physics of the problem. Although the Reynolds number in this range is close to the critical value, Anderson, Mcgillis & Grosenbaugh (2001) showed experimentally that the flow attached to the fish remains laminar.

An oscillating plate is an efficient simplified model representing the complex fluid mechanics of fish fins (Combes & Daniel 2001; Liu & Aono 2009; Kolomenskiy *et al.* 2011; Alben *et al.* 2012). Exploring the hydrodynamics of oscillating plates enables researchers to better understand fish locomotion and to create efficient and manoeuvrable designs for biomimetic underwater swimmers. Early designs of fish-inspired robots include passive rigid or moderately elastic plates of various shapes actuated by servomotors (Triantafyllou & Triantafyllou 1995; Anderson *et al.* 1998). Some designs successfully mimicked the fish flexibility through a series of linked rigid sections coupled to actuators (Su *et al.* 2014). Although such design proved to be successful in propelling robots, not only was the manoeuvring limited compared with what is seen in nature, but the efficiency was far from what fish achieve (Hu *et al.* 2006; Kopman *et al.* 2015).

Recently, internally actuated smart materials have been developed and used to mimic complex fish-like motion showing a great potential for the development of efficient biomimetic swimming robots (Chen, Shatara & Tan 2009; Chen *et al.* 2011; Philen & Neu 2011). Among internally actuated smart materials, piezoelectric materials have gained significant interest. Particularly, macrofibre composite (MFC) piezoelectric actuators strike a balance between the actuation force and deformation levels, in addition to offering robust design and silent operation (Erturk & Delporte 2011). The use of smart materials significantly simplifies the design of bioinspired robotic swimmers. Cen & Erturk (2013) demonstrated a robotic fish propelled by MFC bimorphs, which consists of two MFC laminates bonded together by a layer of epoxy. While MFC bimorphs and other smart materials are highly promising solutions for driving bioinspired designs, they still yield somewhat limited deflection magnitude during underwater actuation due to hydrodynamic loads. Furthermore, it is unclear at what hydrodynamic regimes such materials need to be used to induce efficient locomotion and how their hydrodynamic performance compares with more traditional propulsors actuated by external driving mechanisms.

The problem of elastic plates oscillating in fluid is not limited to the biological and biomimetic locomotion. This fundamental problem has direct implications to a wide range of engineering applications including energy harvesting (Erturk & Inman 2011; Cha, Kim & Porfiri 2013; Sader *et al.* 2016), atomic force microscopy (Van Eysden & Sader 2007; Ghatkesar *et al.* 2008), cooling of electronic devices (Bidkar *et al.* 2009) and the design of offshore structures (Sarpkaya & Isaacson 1981), to name but a few.

The intrinsic complexity of this problem led the researchers to investigate simplified models. Morison, Johnson & Schaaf (1950) suggested that the hydrodynamics of a stationary body in oscillating flow and an oscillating body in quiescent fluid can be represented as a sum of two contributions: the drag and inertial forces. These forces in the Morison equation are characterized by two respective empirical coefficients. Keulegan (1958) and Sarpkaya (1976, 1986) showed that the drag and inertia coefficients depend on the Keulegan–Carpenter number, the aspect ratio, the Reynolds number and the surface roughness. These studies considered only rigid or moderately elastic bodies, yet the deformability is a major parameter in the characterization of the plate hydrodynamic performance (Zhang, Liu & Lu 2010). Nonetheless the Morison equation is a widely used approach to describe forces acting on a submerged elastic body (Kopman *et al.* 2015; Shahab, Tan & Erturk 2015; De Rosis & Lévêque 2016). Lighthill (1960) and Wu (1961) studied two-dimensional inviscid flow induced by a harmonically oscillating rigid plate. Their works laid the foundation of inviscid theory applied to, respectively, slender bodies and infinite thin plates. Lighthill (1970, 1971) studied the reactive forces between an oscillating slender body and a surrounding quiescent fluid. He suggested that the mean thrust depends on the tip angle, tip velocity and mass ratio of the body. Elmer & Dreier (1997) and Van Eysden & Sader (2006) built approximate solutions for cantilevered beams in an inviscid fluid. While providing important insights, the inviscid approximations are of limited use for small-scale problems, where the fluid viscosity cannot be neglected.

Forced resonance oscillations lead to enhanced deflection of elastic cantilevers beneficial in practical applications. Sader (1998) considered resonance of a thin beam with a large aspect ratio subjected to harmonic oscillations in a two-dimensional Stokes flow. His work provided an *a priori* estimation of the beam frequency response and its dependence on the Reynolds number. Aureli, Basaran & Porfiri (2012) used a two-dimensional numerical model to examine the viscous effects on resonance oscillations of a cantilevered beam. Due to the model limitations, this work was not able to capture three-dimensional vortex shedding that accounts for a significant amount of the drag created by the beam motion. More recently, Facci & Porfiri (2013) extended Sader's model to probe three-dimensional nonlinear effects of the fluid–solid coupling. They compared the numerical model with experimental data for a cantilevered beam under harmonic base excitation in a viscous fluid. Their work only considered a linear theory and, therefore, small deformations. Alben *et al.* (2012) demonstrated the existence of resonant-like peaks in swimming velocity through experiments and a high-Reynolds-number theoretical model of an elastic plunging plate. Quinn, Lauder & Smits (2014) experimentally showed that these resonant peaks in thrust occurred for discrete values of the effective flexibility, a non-dimensional parameter measuring the ratio of added mass forces to internal bending forces.

Despite rapid progress in computational modelling, simulations of a three-dimensional fish swimming in a viscous fluid remain a great challenge. Various simplifications are commonly used such as inviscid fluid, rigid and simplified geometry, and prescribed body kinematics (Zhu *et al.* 2002; Borazjani & Sotiropoulos 2008; Mittal *et al.* 2008; Yu *et al.* 2011; Bhalla *et al.* 2013; Li *et al.* 2014; Liu *et al.* 2017). To probe the fundamentals

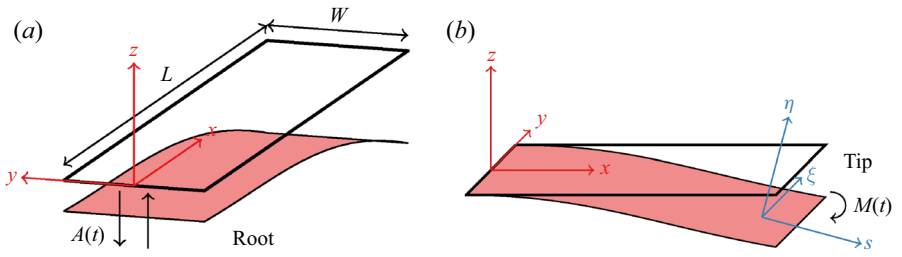

FIGURE 1. Schematics of rectangular elastic plates with (*a*) external and (*b*) internal actuation methods in the global and local reference frames. The externally actuated plate is driven at the root by harmonic oscillations with an amplitude $A(t)$. The internally actuated plate is driven by a time-dependent distributed internal bending moment $M(t)$.

of fish locomotion, a single fin abstraction is used in fully coupled studies probing the hydrodynamics of heaving elastic fins (Eloy & Schouveiler 2011; Dai *et al.* 2012). Such studies showed that resonance oscillations of elastic fins promote propulsion speed and thrust generation (Yeh & Alexeev 2014; Paraz, Schouveiler & Eloy 2016; Yeh & Alexeev 2016*b*). Furthermore, elasticity can be used to optimize fin performance (Hoover *et al.* 2018). Comparison of cruising speed of elastic plates with different shapes revealed that the contracting fin shape facilities a faster swimming in comparison to fins with the diverging shape (Engels *et al.* 2017). It was also reported that fins with tapered thickness yield greater efficiency for a wider range of actuation frequencies than fins with uniform thickness (Yeh, Li & Alexeev 2017). Simulations of internally actuated fins with passive fin attachments revealed that such attachments yield improved hydrodynamic performance (Yeh & Alexeev 2016*a*).

While different aspects of the hydrodynamic performance of heaving elastic fins have been extensively studied, little progress has been achieved so far in understanding the hydrodynamics of plates with internal actuation, such as MFC and other smart materials. In this work, we aim to reduce this gap by combining three-dimensional computer simulations and experiments. We systematically investigate the hydrodynamic performance of rectangular elastic plates with uniform thickness that are driven to oscillate by a distributed time-varying internal bending moment and compare this performance against the performance of plates with similar mechanical and geometrical properties that are actuated by an external force imposed at the root to generate plunging motion (figure 1). We focus on resonance plate oscillations at moderate Reynolds numbers in the range $500 < Re < 4000$. We first use the experiments to validate the kinematics predicted by our fluid–structure model for internally and externally actuated plates with a tip deflection $\delta_t/L = 0.01$, where L is the plate length. We then employ our simulations to probe how the two distinct actuation mechanisms affect the emerging flow structures and generated hydrodynamic forces for a wide range of tip deflections $0.001 < \delta_t/L < 0.25$ that covers both the linear and nonlinear oscillation regimes. We consider plates with different aspect ratios and vary the Reynolds number to probe its effect on the resonance plate hydrodynamics. We also quantify the inertia coefficient characterizing resonance oscillations of the internally and externally actuated plates, and compared it with the experimental data.

2. Problem set-up

We consider a thin elastic plate with length L, width W and uniform thickness $h \ll L$ yielding an aspect ratio $\mathcal{A}_\mathcal{R} = L/W$ shown in figure 1. The plate oscillates periodically

Actuation period	τ	2000
Density	ρ	1
Viscosity	μ	1.25×10^{-3}
Reynolds number	Re	$\dfrac{U_0 L}{\nu} = 1000$
Mass ratio	χ	$\dfrac{\rho W}{\rho_s h} \in \{1; 10\}$
Aspect ratio	$\mathcal{A}_\mathcal{R}$	$\dfrac{L}{W} \in \{2; 4\}$

TABLE 1. Simulation parameters.

in an incompressible Newtonian fluid of density ρ and dynamic viscosity μ. We consider two different configurations of the plate actuation. In the first configuration, referred to as an externally actuated plate, the elastic plate is actuated at its root with a harmonic plunging pattern given by $A(t) = A_0 \sin \omega t$, where ω is the angular velocity, A_0 is the root displacement amplitude and t is time. In the second configuration, referred to as an internally actuated plate, the plate is driven by a harmonic internal bending moment given by $M(t) = M_0 \sin \omega t$, with M_0 being the moment amplitude in the y-direction. In the internally actuated configuration the plate root is clamped and fixed in place. In both cases, the plate material is isotropic and homogeneous with the density ρ_s, the bending stiffness D and the Poisson ratio ν.

The plate oscillations in a fluid are governed by the Reynolds number $Re = \rho U_0 L/\mu$ and the mass ratio $\chi = \rho W/\rho_s h$. Here, $U_0 = L/\tau$ is the characteristic oscillation velocity and $\tau = 2\pi/\omega$ is the actuation period. Additionally, we define a characteristic force $F_0 = (\rho W L U_0^2)/2$ and power $P_0 = (\rho W L U_0^3)/2$. The simulation parameters are summarized in table 1 with the dimensional parameters given in LB units.

The added mass is characterized by an inertia coefficient $c_m = 4/(\pi\chi)(\omega_{1,vac}^2/\omega_{1,f}^2 - 1)$ that is a function of the mass ratio and frequency ratio (see appendix A). For small enough oscillation amplitudes, the inertia coefficient only varies with the plate aspect ratio. We refer to this regime as the linear regime. For greater amplitudes, nonlinear hydrodynamic effects make the inertia coefficient vary with the tip amplitude in addition to the aspect ratio (Shahab *et al.* 2015; Tan & Erturk 2018). We refer to the latter behaviour as the nonlinear regime.

The dynamic response of an oscillating elastic plate is a function of the proximity of the driving frequency to the plate resonance frequency. The resonance frequency depends on the properties of the plate material as well as the fluid surrounding the plate. In vacuum and by neglecting internal dissipation (structural damping), small deflections of a beam with bending rigidity D and mass per length $M_l = \rho_s W h$ can be modelled by

$$M_l \frac{\partial^2 w}{\partial t^2} + D \frac{\partial^4 w}{\partial x^4} = 0. \tag{2.1}$$

This problem can be solved using Fourier decomposition (Weaver Jr., Timoshenko & Young 1990) yielding the natural frequencies $\omega_{n,vac}$ given by

$$\omega_{n,vac} = \frac{\lambda_n^2}{L^2}\sqrt{\frac{D}{M_l}}, \tag{2.2}$$

where λ_n is an eigenvalue of the problem, $n \in \mathbb{N}^*$ and the first vibration mode, $n = 1$, is of interest in this work. The natural frequency, corresponding to the condition when the response and excitation are in quadrature of phase, yields the maximum tip deflection. In the lightly damped problem, such as the vacuum case, the resonance frequency is approximately the natural frequency. Fluid displaced by the oscillating plate acts as an additional mass altering the dynamics of the plate. When the added mass is significantly greater than the plate mass, the effective linear mass due to the displaced fluid can be used instead of the plate mass. This leads to a dimensionless effective flexibility $D^* = (\rho W f^2 L^5/D)^{1/2}$ representing the ratio of added mass forces to internal bending forces (Quinn *et al.* 2014).

When the plate is driven to oscillate in a fluid, the resonance frequency defines the oscillation regime maximizing the tip deflection. Fluid viscosity affects the forced resonance frequency, although for low fluid damping the resonance frequency overlays with the natural (undamped) frequency. Note that Quinn *et al.* (2014) and Hoover *et al.* (2018) have shown for elastic plates that the maxima of the thrust and tip deflection occur for the same effective flexibility. Thus, the values of D^* corresponding to the maximum thrust match the forced resonance frequency. We also note that experimentally the frequency sweep is performed by varying the actuation frequency. In our numerical simulations, however, the actuation frequency is constant, whereas the stiffness is varied to alter the proximity of the oscillating plate to the resonance frequency.

3. Computational set-up

Our computational model is based on a fully coupled solver simulating the three-dimensional hydrodynamics of an elastic plate submerged into an incompressible Newtonian fluid. The fluid mechanics of plate oscillations is captured using a lattice Boltzmann (LB) model, while the solid mechanics is solved using a finite differences (FD) formulation.

The LB method is based on the solution of the discrete Boltzmann equation. The computational domain is discretized using a cubic lattice of equally spaced nodes. At each node, the flow is characterized by a velocity distribution function $f_i(\boldsymbol{r}, t)$ that represents the density of fluid particles at position $\boldsymbol{r}$ propagating at velocity $\boldsymbol{c}$ in the direction i at time t. We use a D3Q19 lattice that maintains 19 directions of the distribution function in three spatial dimensions. The time evolution of the distribution function is computed by integrating the discrete Boltzmann equation (Ladd & Verberg 2001). The macroscopic quantities characterizing the flow, such as the density ρ, momentum $\rho\boldsymbol{u}$ and stress $\boldsymbol{\Pi}$ are retrieved by taking moments of the distribution function given by

$$\rho = \sum_i f_i, \quad \rho\boldsymbol{u} = \sum_i f_i \boldsymbol{c}_i, \quad \boldsymbol{\Pi} = \sum_i f_i \boldsymbol{c}_i \otimes \boldsymbol{c}_i. \tag{3.1a–c}$$

The plate elastic deformation is modelled using the Kirchhoff–Love approach (Timoshenko & Woinowsky-Krieger 1959) with the x, y and z components of plate

displacement (figure 1) defined, respectively, as

$$\left.\begin{aligned} u(x, y, z) &= -z\frac{\partial w}{\partial x}(x, y), \\ v(x, y, z) &= -z\frac{\partial w}{\partial y}(x, y), \\ w(x, y, z) &= w(x, y, 0) = w(x, y). \end{aligned}\right\} \tag{3.2}$$

For a differential plate element of size dx and dy, the forces and moments acting on the element are given by

$$\frac{\partial M_x}{\partial x} + \frac{\partial M_{xy}}{\partial y} = Q_x, \tag{3.3}$$

$$\frac{\partial M_{xy}}{\partial x} + \frac{\partial M_y}{\partial y} = Q_y, \tag{3.4}$$

$$\frac{\partial Q_x}{\partial x} + \frac{\partial Q_y}{\partial y} + q(x, y, t) = \rho_s h\frac{\partial^2 w}{\partial t^2}. \tag{3.5}$$

Here, Q_x, Q_y and M_x, M_y are the shear forces and bending moments in the respective direction, M_{xy} is the twisting moment and q is the transverse load acting on the plate. For an isotropic material, the bending moments are given by

$$M_x = -D\left(\frac{\partial^2 w}{\partial x^2} + \nu\frac{\partial^2 w}{\partial y^2}\right), \tag{3.6}$$

$$M_y = -D\left(\frac{\partial^2 w}{\partial y^2} + \nu\frac{\partial^2 w}{\partial x^2}\right), \tag{3.7}$$

$$M_{xy} = -D(1-\nu)\frac{\partial^2 w}{\partial x\partial y}, \tag{3.8}$$

where $D = Eh^3/12(1-\nu^2)$ is the bending stiffness of the plate, which is constant considering an isotropic plate with constant thickness. By combining (3.3)–(3.8), we obtain an equation for the transverse displacement of the elastic plate

$$\rho_s h\frac{\partial^2 w}{\partial t^2} = q(x, y, t) + \left(N_x\frac{\partial^2 w}{\partial x^2} + N_y\frac{\partial^2 w}{\partial y^2} + N_{xy}\frac{\partial^2 w}{\partial x\partial y}\right) - D\nabla^4 w - \gamma\nabla^4\frac{\partial w}{\partial t}, \tag{3.9}$$

where ∇^4 is the bilaplacian operator, $\gamma \geqslant 0$ is the Kelvin–Voigt damping coefficient and N_x, N_y, N_{xy} are the in-plane shearing forces. The partial differential equation is completed with the following boundary conditions:

$$\left.\begin{aligned} w(0, y, t) = B \wedge \frac{\partial w}{\partial x}(0, y) = 0&\text{: clamped root,} \\ M_x(L, y) = 0 \wedge V_x(L, y) = 0&\text{: free tip,} \\ M_y(x, 0) = 0 \wedge V_y(x, 0) = 0&\text{: free side,} \\ M_y(x, w) = 0 \wedge V_y(x, w) = 0&\text{: free side.} \end{aligned}\right\} \tag{3.10}$$

Here, $B = A(t)$ for the externally actuated plate, whereas in the case of the internally actuated plate, $B = 0$. Furthermore, $V_x(x, y) = Q_x(x, y) + \partial M_{xy}/\partial y(x, y)$ is

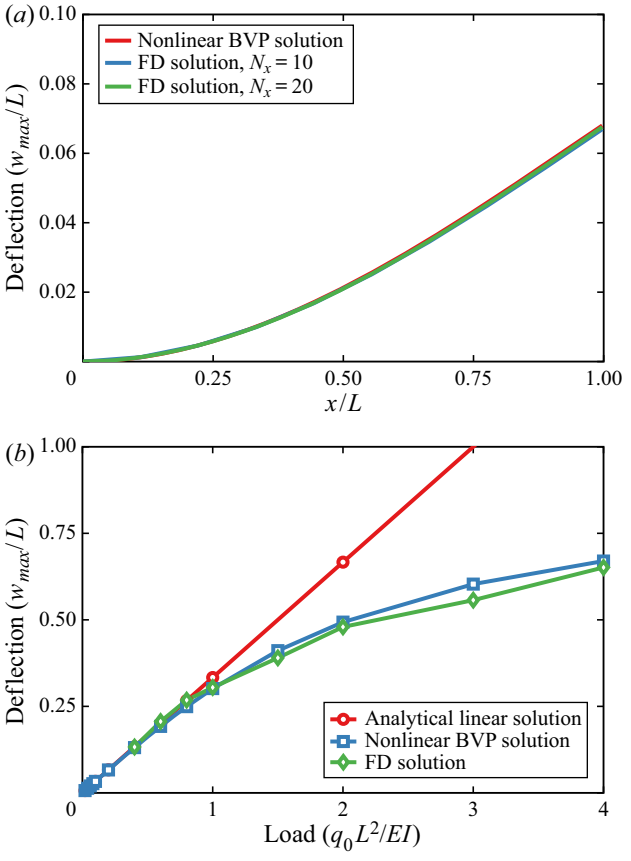

FIGURE 2. (*a*) Bending deformation of the end-loaded cantilevered plate with aspect ratio $\mathcal{A}_\mathcal{R} = 2$ and a non-dimensional load $q_0L^2/EI = 0.2$. The FD solution using 20 node mesh deviates less than 1 % from the nonlinear BVP solution. (*b*) Static deflection of the end-loaded cantilevered plate with aspect ratio $\mathcal{A}_\mathcal{R} = 2$ as a function of the non-dimensional load q_0L^2/EI. The comparison between the nonlinear Runge–Kutta and the FD solutions shows good agreement including for moderate to high deformation levels. The linear analytical solution only valid for relatively small loads.

the equivalent shear force, which was introduced by Kirchhoff (1850) to reduce the number of boundary conditions to two. The corner reaction is defined as

$$R = 2M_{xy}(x, y) = -2D(1-\nu)\left.\frac{\partial^2 w}{\partial x\,\partial y}\right|_{x,y}. \tag{3.11}$$

We solve the plate equation of motion with relevant boundary conditions using FD. The time and space discretization is based on a central FD scheme with ghost nodes at the boundaries. This choice of the discretization results in a 13 point stencil. We validated the FD solid solver by modelling static deflection of a cantilevered plate due to a load applied at the free end. The numerical solution is compared with the deflection of an Euler–Bernoulli beam with a bending stiffness *EI* described by the following boundary

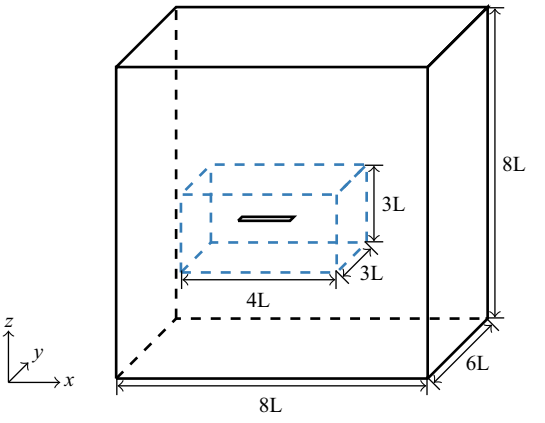

FIGURE 3. Schematic of the computational set-up. The outer box represents the domain with the coarse LB model grid while the inner box represents the domain with the fine LB model grid centred around the oscillating elastic plate.

value problem (BVP):

$$\forall s \in]0;\, 1[,\, \theta''(s) = -\frac{q_0 L^2}{EI}\cos\theta(s), \tag{3.12}$$

$$\theta(0) = 0, \quad \theta'(1) = 0, \tag{3.13a,b}$$

where q_0 is the load, s is the arclength coordinate, L is the length of the beam and θ is the beam angle. The equation is solved using a fourth-order Runge–Kutta scheme.

In figure 2, we show the bending pattern of an end-loaded cantilevered plate of aspect ratio $\mathcal{A}_\mathcal{R} = 2$ for a non-dimensional load of $q_0 L^2/EI = 0.2$. Our FD solution shows good agreement with the Runge–Kutta solution. In figure 2, the beam solution is compared with our FD solution for various loads. We find close agreement between the finite differences results and the Runge–Kutta solution with tip deflections reaching up to 70 % of the beam length for a mesh of 20 nodes in length and 11 nodes in width.

To simulate the fluid flow, we use a grid with reduced density away from the moving plate to decrease the computing time for this fully coupled fluid–structure interaction problem. The coarse grid spacing is $\Delta_c = 2$ while the fine grid spacing is $\Delta_f = 1$ in LB units. Dimensions of the domains are shown in figure 3. The fine and coarse grids are coupled at their boundaries to ensure the mass and momentum conservation (Masoud & Alexeev 2010). The plate is located at the centre of the fluid domain. The outer boundaries of the computational domain are located far enough from the plate so that the boundary conditions do not influence the flow field near the oscillating plate. Based on the results of a mesh sensitivity study of the coupled LB/FD model, we use an FD mesh of 21 nodes in the x-direction that corresponds to 50 LB grid units. Such mesh provides sufficient accuracy compared with the solution with higher mesh resolution at reasonable computational cost. To ensure that the plate reaches a steady state, the simulations are performed for 40 periods of the plate oscillations.

The fluid and solid models are coupled at the fluid–solid boundaries using a two-way coupling procedure (Alexeev, Verberg & Balazs 2005; Alexeev & Balazs 2007). On the fluid side, a linear interpolated bounceback rule is used that results in the no-slip and no-penetration conditions on the moving solid surface (Bouzidi,

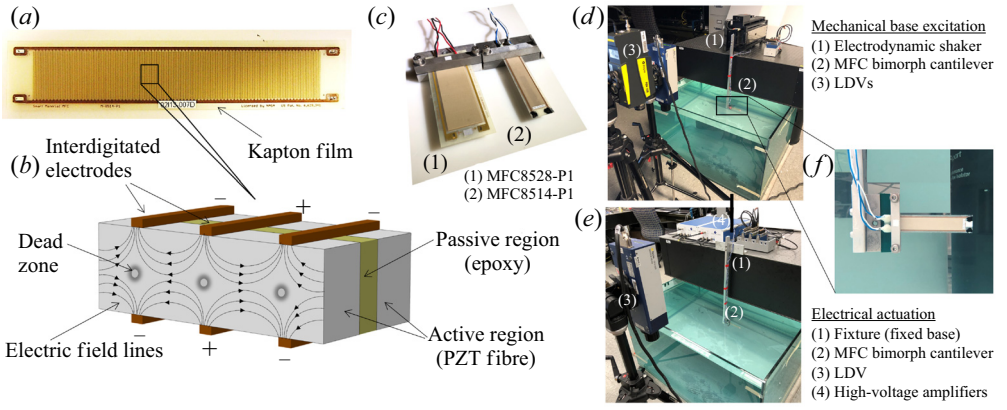

FIGURE 4. Picture of (*a*) an MFC laminate and (*b*) close-up schematic of a representative volume element showing the interdigitated electrodes, piezoelectric fibres and epoxy matrix embedded in Kapton film. (*c*) Bimorph cantilevers with two different aspect ratios (each made from two MFC laminates for bending actuation). (*d*) Mechanical base excitation (external actuation) set-up and (*e*) electrical (internal) actuation set-up. (*f*) Close-up view of an MFC bimorph cantilever.

Firdaouss & Lallemand 2001; Chun & Ladd 2007). The rule is applied to all distribution functions crossing the solid boundary. On the other hand, the momentum exchange approach (Alexeev *et al.* 2005) is used to account for the momentum transferred to the solid boundary due to the reflection of the distribution function. This momentum is distributed among neighbouring FD nodes using a weighted average conserving force and moment.

This fluid–solid interaction framework has been previously extensively validated and used to study diverse problems involving coupling between viscous fluids and elastic solids (Alexeev, Verberg & Balazs 2006; Branscomb & Alexeev 2010; Masoud & Alexeev 2011; Masoud, Bingham & Alexeev 2012; Mao & Alexeev 2014; Yeh & Alexeev 2014). Below we further validate the coupled fluid–structure interaction solver by directly comparing the simulation results with experimental measurements for externally and internally actuated plates.

4. Experimental set-up

The experimental test samples (piezoelectric cantilevers) and the overall set-up details are shown in figure 4 along with close-up views of the relevant components. The geometrical and structural parameters for the samples are listed in table 2. The flexible piezoelectric structures were built by vacuum bonding a pair of the identical custom-made waterproof MFC laminates using high strength epoxy (3M DP460) to fabricate bimorph structures. Electrical wires were soldered to the electrodes of the MFCs and the joint was fully waterproofed by multiple layers of liquid electrical tape (Star Brite Liquid Electrical Tape). Two different excitation mechanisms of input energy are applied to create persistent oscillations of the cantilevers: electrical (internal) actuation and mechanical (external) base excitation.

First, in the piezoelectric actuation, the bimorphs were placed into an aluminium clamp attached to a rigid mount to create a cantilevered structure and electrically connected to a pair of high voltage amplifiers (Trek PA05039). Linear electrical actuation experiments were conducted with the sample in a vacuum chamber to characterize the dynamics of

$\mathcal{A}_\mathcal{R}$	L (mm)	W (mm)	h (mm)	ρ_s (kg m^{-3})	D (N m^2)	χ
2	88.5	43.5	6.1	360	0.0163	20
4	83.5	21.5	6.1	360	0.087	10

TABLE 2. Experimental parameters.

the structure in the absence of fluid loading. To do so, electrical noise bursts were sent to the piezoelectric bimorphs while the mechanical response at the tip of the cantilever was measured using a laser Doppler vibrometer (LDV) (OFV-5000 with an OFV-505 sensor head). Once the linear response was well-characterized along with *in vacuo* structural damping, frequency sweeps were conducted around the first resonant frequency to measure the amplitude dependence between the piezoelectric bimorph and the surrounding fluid. Later, the structure was submerged underwater to a depth of 25 cm to avoid surface effects. Linear electrical actuation experiments were repeated under water, being careful to divide the measured tip velocity underwater by the index of refraction of water to determine the true velocity of the structure. By comparing the dynamics of the structural modes from the *in vacuo* and underwater experiments, empirical linear inertia coefficients were extracted from the data. Once the linear tests were complete, the nonlinear response of the structure was again measured via frequency sweeps underwater centred around the first resonant frequency of the underwater structure.

For mechanical external actuation experiments, the bimorphs (along with the aluminium clamps) were fixed onto the testing platform of an APS-113 long-stroke shaker which was connected to an APS-125 amplifier. For the sake of the characterization of the dynamic response of the bimorphs under mechanical external actuation, linear *vacuo* tests were again conducted in a vacuum chamber to have a reference for obtaining the inertia coefficient. An LDV was used for obtaining the absolute tip velocity of the bimorphs and, at the same time, another LDV was implemented to collect the velocity-to-actuation voltage input frequency response from the fixed end of the bimorphs. After the *in vacuo* reference experiments, the bimorphs were immersed in water along with an aluminium bar that had one of its ends attached to the shaker. Similarly, linear mechanical actuation tests were done to characterize the dynamics of the bimorphs to characterize fluid loading effects. Finally, large-amplitude frequency sweeps were conducted in the frequency range centred around the first resonant frequency obtained from the prior tests. Note that to keep the oscillation level at the fixed end of the bimorphs constant within the entire range of frequency sweeps, the velocity signals obtained from the second LDV were sent into a controller to create a closed-loop feedback control system as required in nonlinear vibration experiments. Typical characteristic velocities lead to a Reynolds number in the range between 10^2 and 10^4.

5. Results and discussion

5.1. *Resonance oscillations*

In figures 5 and 6, we present simulation results and experimental data for internally and externally actuated plates oscillating in water with a moderate tip deflection $\delta_t/L = 0.01$. Close agreement between the simulations and experiments confirms the ability of our coupled fluid–structure interaction solver to properly model such oscillations. Figure 5 shows the Bode diagrams for plates with external and internal actuation. The phase $\Delta\theta$

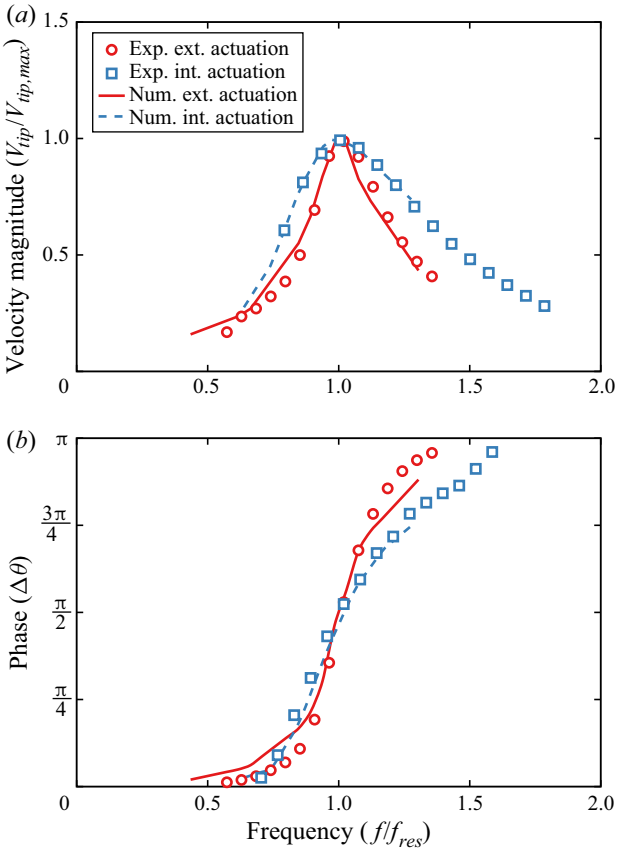

FIGURE 5. Frequency response function for (a) the tip velocity V_{tip} and (b) the phase for in water oscillations with $\delta_t/L = 0.01$, $\chi = 5$ and $\mathcal{A}_\mathcal{R} = 2$. The numerical results are shown by the lines, whereas the experimental data are shown by the symbols. The resonance is characterized by a quadrature of phase $\Delta\theta = \pi/2$ between the root and the tip.

is computed as the lag between the root and tip displacements for the externally actuated plate. In the case of the internally actuated plate, $\Delta\theta$ is computed as the lag between the tip displacement and the input internal moment.

As the driving frequency approaches the resonance frequency of the plate, the tip velocity magnitude and, therefore, tip displacement reach a maximum (figure 5*a*). The resonance frequency can therefore be identified by inspecting the root mean square tip velocity V_{tip} frequency response. On the other hand the natural frequency can be identified by investigating the phase difference between the driving source (root displacement or internal moment) and the tip deflection. At the natural frequency the driving source and tip displacement are in quadrature of phase (figure 5*b*). For the amplitude $\delta_t/L = 0.01$, the natural and resonance frequency coincide, confirming that the plate oscillates in the linear regime.

In this work, we focus on the hydrodynamics of resonance oscillations. In figure 6, we show experimental and computational snapshots illustrating the plate bending pattern and corresponding plate curvature $\kappa(x) = z''(x)/[1 + z'^2(x)]^{3/2}$ for the internally and externally actuated plates. The plate aspect ratio is $\mathcal{A}_\mathcal{R} = 2$ and the actuation in both cases yields $\delta_t/L = 0.01$. In the case of an external actuation, the plate deformation in

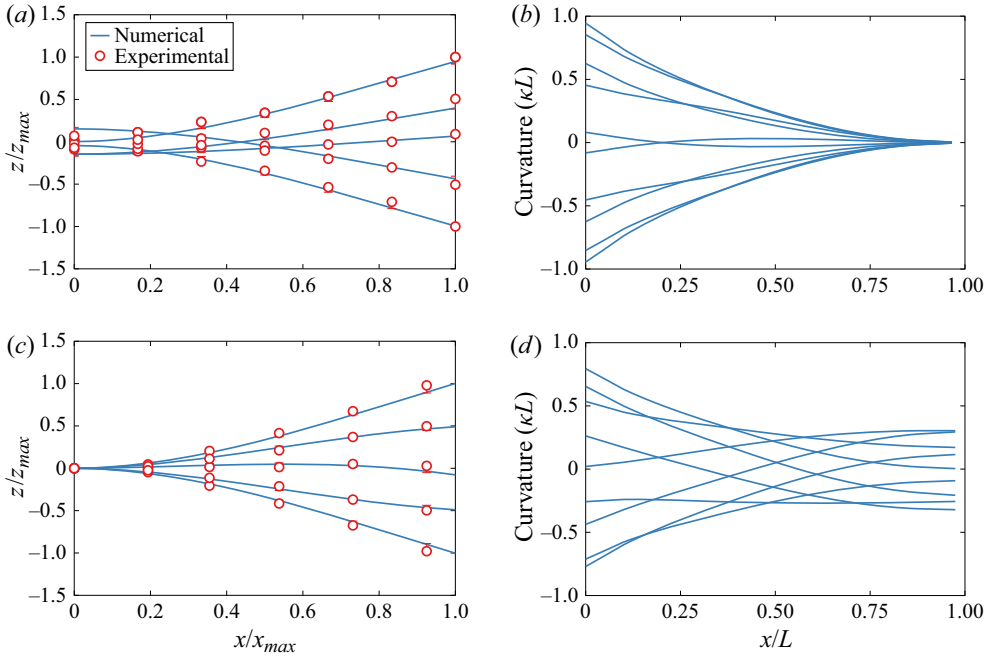

FIGURE 6. (*a*) Plate bending pattern and (*b*) bending curvature κ for the externally actuated plate at resonance. (*c*) Plate bending pattern and (*d*) bending curvature κ for the internally actuated plate at resonance. Numerical results are shown by the solid lines, whereas experimental data are shown by the symbols. The plates oscillate in water, the plate tip displacement is $\delta_t/L = 0.01$, the aspect ratio is $\mathcal{A}_\mathcal{R} = 2$, $\chi = 5$ and $Re = 1000$.

the z-direction grows monotonically along the plate length with the maximum at the plate free end (figure 6*a*). Such deformation is typical for resonance oscillations. This is confirmed by inspecting the plate curvature (figure 6*b*). The curvature monotonically decreases towards the plate tip from the maximum value at the root. The application of the external force at the root yields the most significant plate bending that gradually decreases towards the tip where the curvature is zero, indicating that near the tip the plate remains straight during the entire oscillation cycle.

The resonance deformation of an internally actuated plate (figure 6*c*) is noticeably different from that of an externally actuated plate. In the case of the internal actuation, the tip of the plate displays a non-zero curvature during most of the oscillation cycle (figure 6*d*). Interestingly the maximum curvature occurs at the plate root for both types of actuation. As we discuss below, the difference in the deformation patterns between externally and internally actuated plates have a drastic effect on the plate hydrodynamics and the generated hydrodynamic forces.

We further compare the plate bending patterns for the two actuation methods in figure 7, where we show the simulated time histories of the plate deflection, the plate rotational angle and the plate curvature. The instantaneous tip deflection $d_t(t)$ and centre of mass displacement $d_{cg}(t)$ are shown in figure 7(*a*). The solid lines refer to the externally actuated case while the dotted lines refer to the internally actuated plate. The maximum tip deflection occurs at approximately $t/\tau = 0.5$ for both the plates, since the plates oscillate at resonance. In the case of the externally actuated plate the centre of mass and the tip

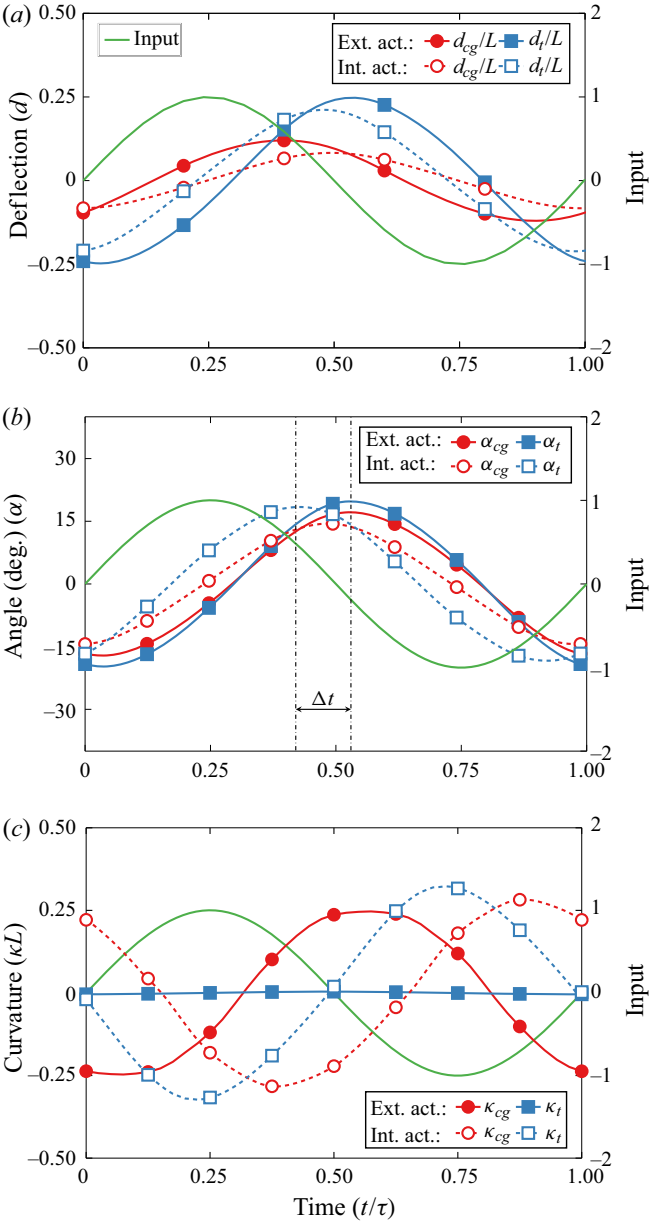

FIGURE 7. Time history of (a) the instantaneous deflection at the tip d_t and at the centre of mass d_{cg}, (b) the angle at the tip α_t and at the centre of mass α_{cg} and (c) the curvature at the tip κ_t and at the centre of mass κ_{cg} for numerically simulated internally actuated (int. act.) and externally actuated (ext. act.) plates with aspect ratio $\mathcal{A}_\mathcal{R} = 2$, $\chi = 5$ and $Re = 1000$ at resonance.

displacement have a phase lag of $\Delta\theta = \pi/4$, while the internally actuated plate centre of mass and tip are in phase.

In figure 7(b), we present the time history of the local plate angle α at the plate centre of mass and tip. For the external actuation, we find that the angle is in phase at both locations. Therefore at the maximum tip displacement, the angle is positive yielding a slope that

effectively transfers the fluid backwards and minimizes the relative motion between the plate and the fluid. On the other hand, for the internally actuated plate, the local angle shifts along the length of the plate so that at the tip the angle and the deflection are out of phase. This change along the length results in relative motion between the plate and the fluid leading to a greater vorticity generation as we discuss below.

In figure 7(*c*), we show the time history of the plate local curvature κ at the centre of mass and at the tip. The externally actuated plate maintains zero curvature at the tip during the entire oscillation period, whereas the curvature at the centre of mass is maximized at the maximum plate deflection. For the internal actuation case, the magnitude of the curvature does not decrease with the distance from the root as it happens for the externally actuated plate. Figure 7(*c*) shows that the curvature magnitude changes insignificantly between the centre of mass location and the trailing edge. Furthermore, the maximum curvature at the tip coincides with the maximum input bending moment to satisfy the respective boundary condition.

5.2. *Flow structure*

In figure 8, we show surfaces of constant vorticity magnitude generated at resonance by externally and internally actuated plates as predicted by our simulations. Vorticity is generated as a result of the relative motion of the plate with respect to the surrounding fluid and, therefore, is the most significant along the trailing edge (TEVs) and the side edges (SEVs) of the plate. During each stroke the combination of SEVs and TEVs forms a characteristic horseshoe shaped set of vortices that are periodically shed from the oscillating plate. The horseshoe vortices sharing common features are generated by plates with both modes of actuation. However, there are also important differences in the emerging flow structures associated with their distinct bending patterns.

Several theoretical and experimental studies highlight the key role of reverse Kármán streets for propulsion (Nauen & Lauder 2002; Alben 2009; Michelin & Llewellyn Smith 2009). Both actuation patterns lead to the generation of sets of vortices with opposite rotation direction. In both instances, anticlockwise vortices are shed at the top while clockwise rotating vortices are shed at the bottom. The direction of these vortices creates a jet flowing away from the tip of the plate. This configuration leads to the production of a net thrust. For the lowest actuation levels tested, the sign of these vortices flip which corresponds to a net drag force on the plate (Anderson *et al.* 1998; Nauen & Lauder 2002; Alben 2009; Michelin & Llewellyn Smith 2009; Paraz *et al.* 2016).

When considering the external actuation, the plunging motion of the plate leading edge produces a leading edge vortex (LEV), however, its strength is relatively weak compared with SEVs and TEV. Since the plate is actuated in a quiescent fluid, the LEVs shed close to the root and do not interact in the wake with TEVs and SEVs. Therefore, we do not anticipate they play an important role in the thrust production for this set-up. Furthermore, SEVs extend along the entire plate length from the root to the tip. In the case of the internal actuation, the root is immobilized. As a result, the internally actuated plate does not produce LEVs, whereas significant SEVs develop only at a halfway distance from the root to the tip. Thus, one can expect the externally actuated plate that displaces more fluid during each stroke would generate more vorticity compared with the internally actuated plate with comparable trailing edge displacement.

To further characterize the flow field, figure 9 shows simulation snapshots of the flow field around oscillating plates with different actuation types. The glyph demonstrates the alternating vortical structure shed at the tip of the plate. A downstroke generates anticlockwise vortices, as shown in figures 9(*b*), 9(*c*), 9(*f*) and 9(*g*), whereas the upstroke

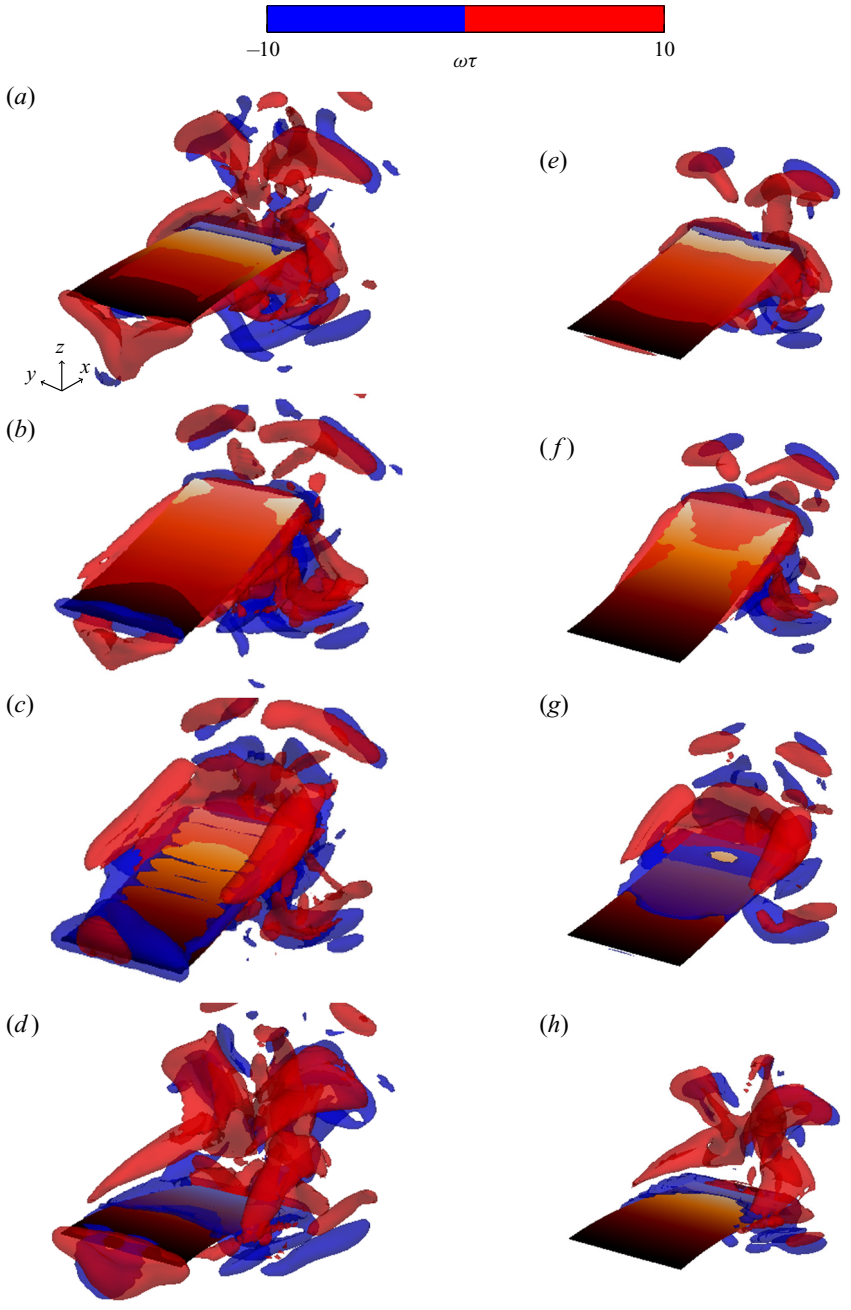

FIGURE 8. Contours of normalized vorticity $\omega\tau = \pm 10$ of the numerically simulated (*a–d*) externally actuated plate and (*e–h*) internally actuated plate with $\mathcal{A}_{\mathcal{R}} = 2$, $\chi = 5$, $Re = 1000$, and tip deflection $\delta_t/L = 0.25$ at resonance at times $t/\tau = 0.25,\ 0.5,\ 0.75,\ 1$, respectively. Vortices represented in red are rotating anticlockwise while vortices represented in blue are rotating clockwise.

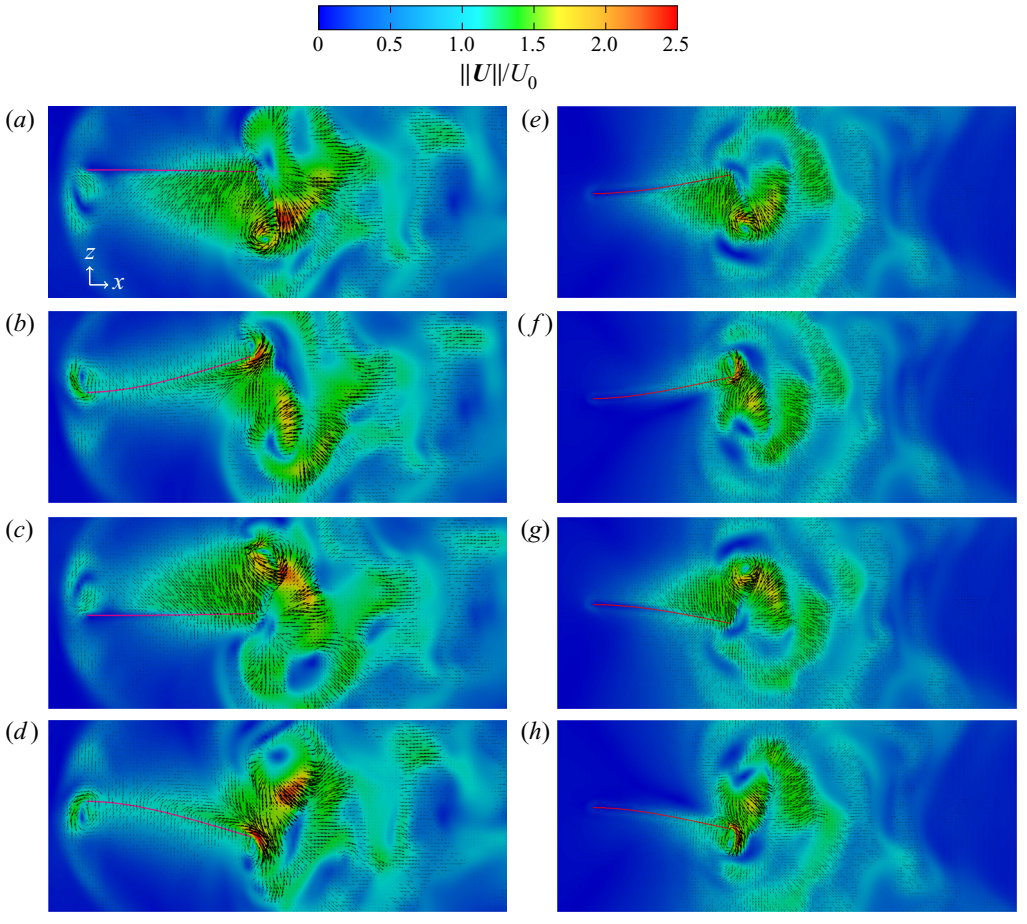

FIGURE 9. Normalized velocity magnitude $||\boldsymbol{U}||/U_0$ of the numerically simulated (*a–d*) externally and (*e–h*) internally actuated plate with $\mathcal{A}_\mathcal{R} = 2$, $\chi = 5$, $Re = 1000$, and tip deflection $\delta_t/L = 0.25$ at resonance at times (*a–d*) $t/\tau = 0.25, 0.5, 0.75, 1$, respectively.

generates clockwise vortices, as shown in figures 9(*a*), 9(*d*), 9(*e*) and 9(*h*) (see also supplementary material available at https://doi.org/10.1017/jfm.2020.915). The interaction of the vortices creates a jet in the x-direction leading to a net thrust. We note that these flow structures are consistent with the literature (Facci & Porfiri 2013).

We quantified the vorticity generated by each actuation method by computing the normalized enstrophy $\mathcal{E} = \boldsymbol{\omega} \cdot \boldsymbol{\omega}\, \tau^2$. Enstrophy is a measure of the intensity of viscous dissipation (Weiss 1991). In figure 10, we show the time evolution of the volume-averaged enstrophy over one period of plate oscillations. For both plates the enstrophy displays similar time-dependent behaviour with two peaks. However, the locations of the peaks are somewhat different. Compared with the plates with external actuation, the peaks for the internally actuated plate shifted towards the ends of the upstroke and the downstroke at $t/\tau = 0.2$ and $t/\tau = 0.7$, respectively. Figure 10 also shows that throughout most of the oscillation period, the internally actuated plate generates noticeable greater enstrophy and, therefore, viscous dissipation compared with the externally actuated plate.

We find that, for the externally actuated plate, the maximum viscous dissipation coincides with the maximum tip deflection, whereas the minimum enstrophy corresponds

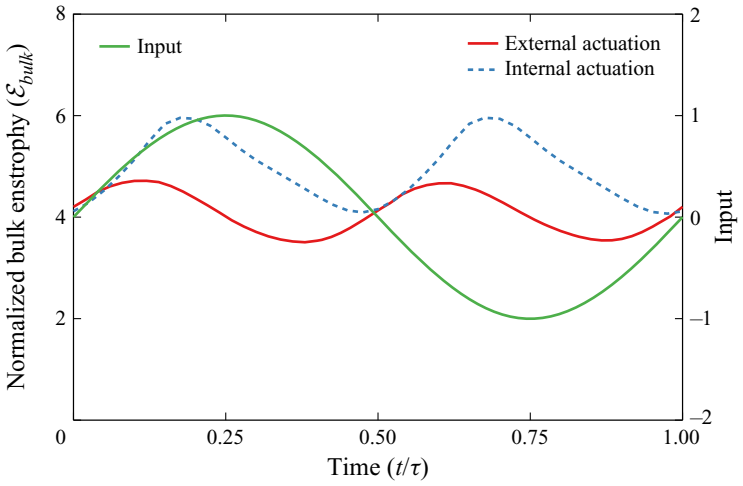

FIGURE 10. Time history of the normalized bulk enstrophy $\mathcal{E}_{bulk}$ for numerically simulated internally and externally actuated plates with $\mathcal{A}_{\mathcal{R}} = 2$, $\chi = 5$, $Re = 1000$, and tip deflection $\delta_t/L = 0.25$ at resonance.

to zero tip deflection (figure 7*a*). In the case of the internally actuated plate, however, enstrophy production is related to the plate curvature at the trailing edge. Indeed, comparing figures 7(*c*) and 10, we find that the maxima of enstrophy are close to the maxima of tip curvature at $t/\tau = 0.25$ and $t/\tau = 0.75$, while the enstrophy minima coincide with zero tip curvature at $t/\tau = 0.5$ and $t/\tau = 1$. Thus, the 'cupping' exhibited by the internally actuated plate is a major contributor causing the increased enstrophy production and, therefore, viscous dissipation.

5.3. *Hydrodynamic forces*

To further investigate the difference between the two actuation methods, we examine time evolution of the hydrodynamic force generated by the plates. In figure 11(*a*), we show the simulation results for the instantaneous lift force F_z over one oscillation period. The input refers to the prescribed motion at the root and the internal moment for the externally and internally actuated plates, respectively. We normalize the forces by the characteristic force based on the plate length. The externally and internally actuated plates yield comparable maximum lift. The maximum occurs close to $\pi/2$ coinciding with the phase of the maximum plate displacement at resonance. The mean lift force is zero due to the symmetry of the periodic oscillations.

The thrust force F_x generated by the plates is presented in figure 11(*b*). The peak-to-peak amplitude of the thrust force is similar for both cases. The difference is, however, that the externally actuated plate generates a significantly greater period-averaged thrust compared with the internally actuated plate. The figure shows that there is almost a twofold difference in the value of the net thrust between the externally and internally plates. We relate this difference to the bending patterns shown in figure 6, where the negative angle at the tip or 'cupping' of the internally actuated plate yields a plate shape that is ineffective for propelling fluid backwards. Thus, the externally actuated plate yields substantially greater thrust than the internally actuated plate with the same tip displacement.

In figure 12(*a*), we plot the dependence of the mean thrust force on the tip deflection δ_t for the externally and internally actuated plates with two different aspect ratios.

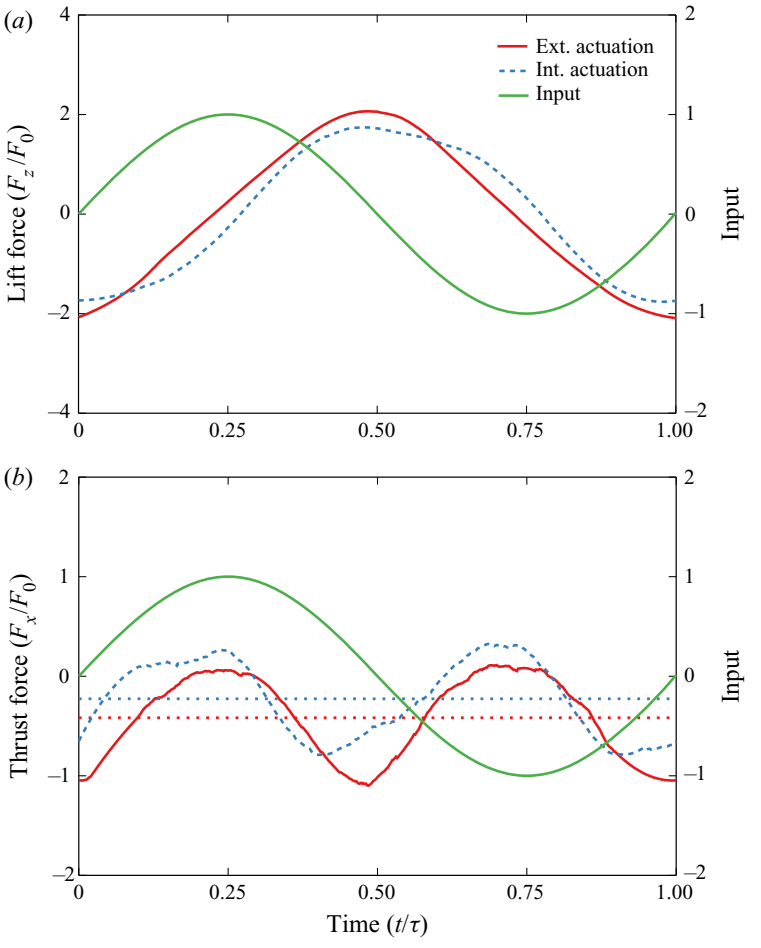

FIGURE 11. Time histories of (*a*) the lift force and (*b*) the thrust force for numerically simulated internally and externally actuated plates with $\mathcal{A}_\mathcal{R} = 2$, $\chi = 5$, $Re = 1000$ and tip displacement $\delta_t/L = 0.25$ at resonance. The horizontal dotted lines show the mean values of the thrust force.

Overall, the normalized thrust increases with the tip deflection. For relatively small δ_t/L (up to approximately 0.05) that roughly corresponds to the linear regime of the plate oscillations, the increase is almost linear with δ_t (see inset in figure 12*a*). For larger values of δ_t, the thrust scales as δ_t^3 indicating the influence of the nonlinear effects. For the two aspect ratios tested, the externally actuated plates generate greater thrust compared with the internally actuated plates. This suggests that externally actuated plates outperform internally actuated plates independently of the aspect ratio given that they have similar trailing edge displacements.

Furthermore, for both the external and internal actuation methods, we find that wider plates with $\mathcal{A}_\mathcal{R} = 2$ produce greater thrust than more narrow plates with $\mathcal{A}_\mathcal{R} = 4$. This difference can be attributed to the effect of SEVs (Raspa *et al.* 2014; Yeh & Alexeev 2016*b*). It was shown using scaling arguments that SEVs increase with the tip displacement, but not the plate width. Therefore, for the same tip displacement a wider plate experiences a weaker adverse effect of SEVs and generates more thrust per plate unit width.

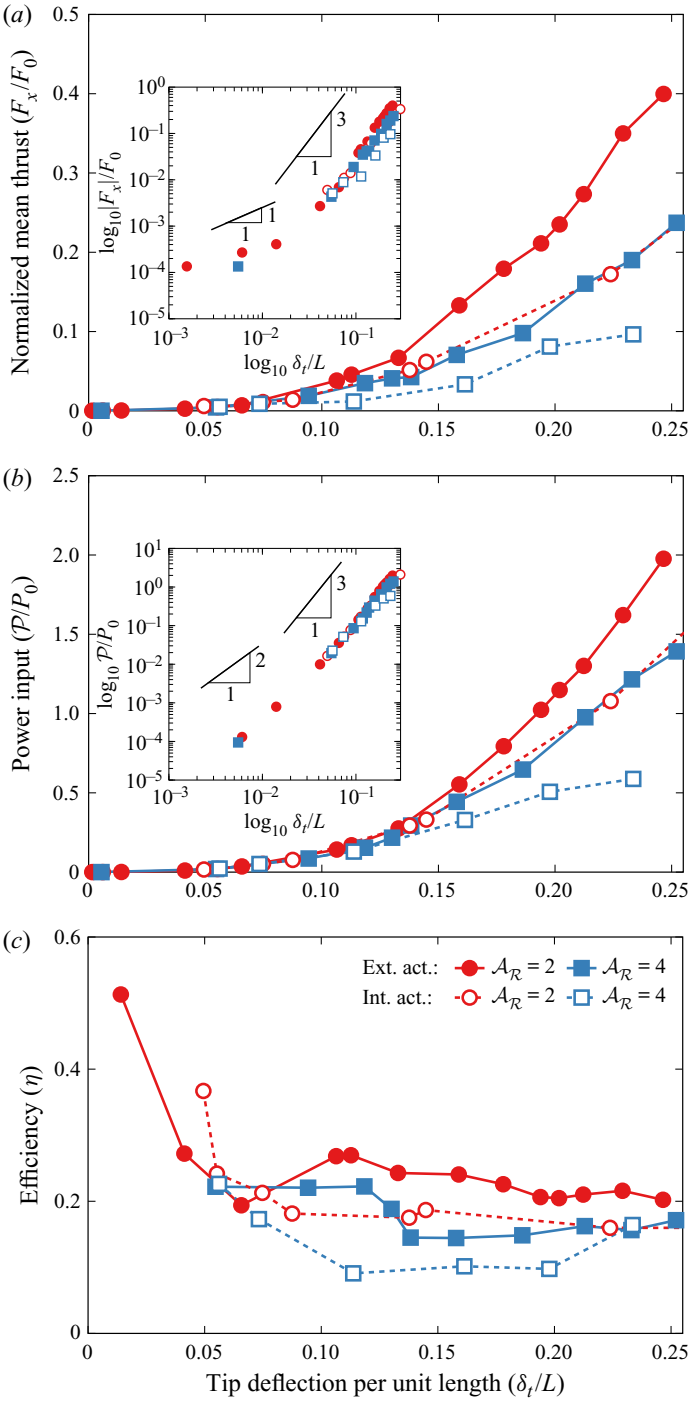

FIGURE 12. Dependence of (*a*) the normalized thrust F_x/F_0, (*b*) input power $\mathcal{P}/P_0$ and (*c*) efficiency η on the tip deflection magnitude δ_t. The simulation results are for $Re = 1000$, $\chi = 5$ and two aspect ratios $\mathcal{A}_\mathcal{R} = 2$ and $\mathcal{A}_\mathcal{R} = 4$.

The power consumption by the internally and externally actuated plates is shown in figure 12(*b*) as a function of the tip deflection δ_t. The power input increases monotonically with the tip deflection for both actuation methods. For small deflection amplitudes $\delta_t/L < 0.05$, the power $\mathcal{P}$ increases proportionally to δ_t^2, whereas for larger δ_t, the power increases as δ_t^3 (see inset in figure 12*b*). We find that the wider plates require greater power input per unit width compared with the narrow plates independently of the actuation method. This is consistent with the higher thrust produced by the wider plates (figure 12*a*) and can be related to larger amounts of fluid displaced by such plates per unit width. Furthermore, we find that externally actuated plates require greater input power to oscillate with the same tip deflection as internally actuated plates. This can be in part attributed to the additional power required by an externally actuated plate to displace fluid near the oscillating plate root compared with the internally actuated plate with clamped root. Indeed, even at small levels of actuation the LEVs and SEVs have comparable sizes (figure 8).

To further characterize the hydrodynamic performance of oscillating plates, we compute the thrust efficiency $\eta = F_x/F_0/\mathcal{P}/P_0$ in figure 12(*c*) as a function δ_t. We find that the efficiency is maximized for smaller δ_t, but rapidly decreases with increasing δ_t within the linear regime. In the nonlinear regime, the efficiency varies slightly with δ_t. Indeed, in the linear regime $F_x \sim \delta_t$ and $\mathcal{P} \sim \delta_t^2$ resulting in $\eta \sim 1/\delta_t$. For greater δ_t characterized by nonlinear oscillations, both F_x and $\mathcal{P}$ scale with δ_t^3, which in turn results in η nearly independent of δ_t. Comparing the externally and internally actuated plates, we find that the externally actuated plates exhibit higher efficiency than the internally actuated plates, except for the lowest tip deflection conditions. This is because at small δ_t the efficiency of the externally actuated plate is reduced due to the plunging motion at the root that dissipates energy but does not contribute to the thrust. For larger values of δ_t, externally actuated plates outperform internally actuated plates with the same aspect ratio. The reduced efficiency of internally actuated plates is associated with the trailing edge curvature disrupting the flow and generating an increased level of vorticity, as shown in figure 10. We also find that wider plates are more efficient than narrow plates for the entire range of δ_t. This is due to the lower contribution of SEVs into the overall energy budget of the wider plates.

In figure 13, we use simulations to probe the effect of the flow regime by varying the Reynolds number for the two actuation methods. Here, we consider plates with two values of tip deflections and $\mathcal{A}_\mathcal{R} = 2$. In figure 13(*a*), we show that the normalized thrust does not change significantly with *Re*. As demonstrated by Lighthill (1970), at high enough *Re* the thrust is mainly defined by the tip kinematics, supported by nearly constant thrust for higher *Re*. Conversely at lower *Re*, the tip kinematics do not fully define the thrust production. This trend persists for both types of actuation, although the externally actuated plates produce greater thrust.

In figure 13(*b*), we show the evolution of the normalized power with *Re*. As the Reynolds number increases the normalized power decreases and remains constant at higher *Re*. This behaviour can be attributed to the increase of viscous dissipation associated with a lower *Re*. To generate the same tip deflection, the plate requires more power when the viscous effects are more significant. For both tested tip deflections, the internally actuated plates consume less power compared with the externally actuated plates.

The change of the hydrodynamic efficiency of the plates with *Re* is shown in figure 13(*c*). Over the entire range of *Re* we tested, the externally actuated plates outperform the internally actuated plates. The difference in efficiency is more significant for the lower tip deflection amplitude. This indicates that as the viscous effects become

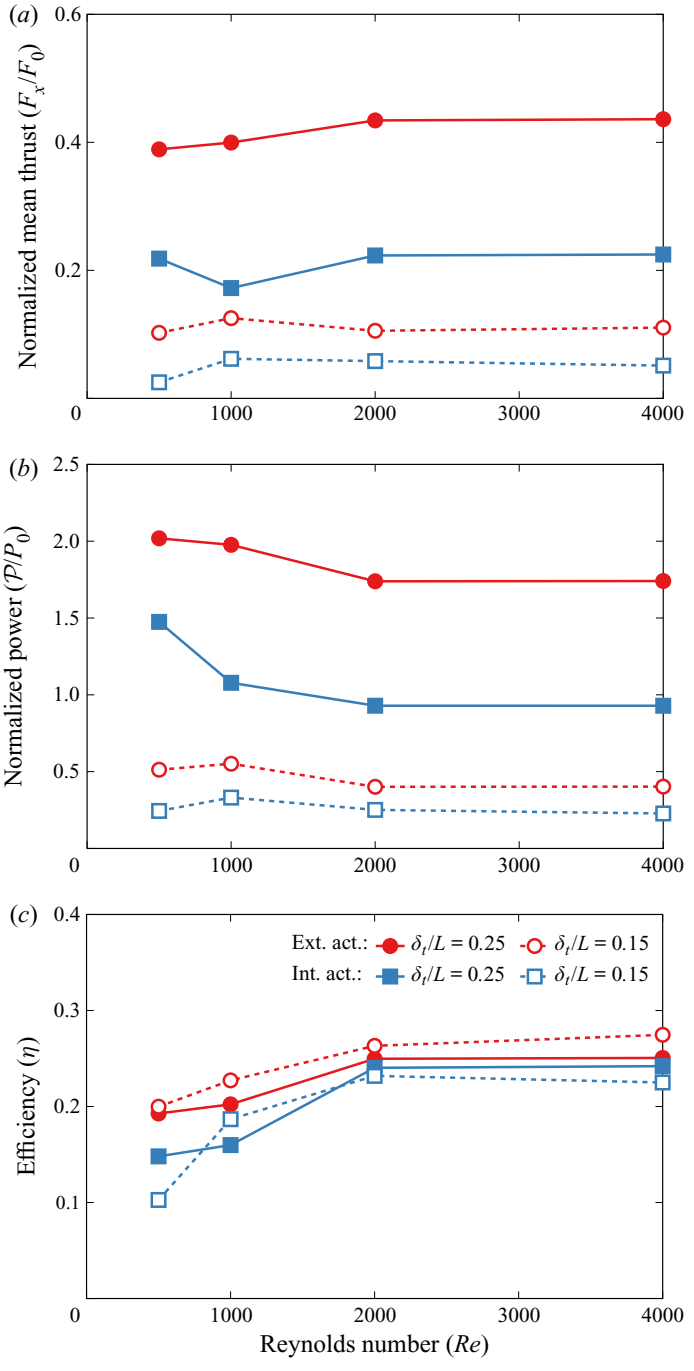

FIGURE 13. Dependence of (*a*) the normalized thrust F_x/F_0, (*b*) input power $\mathcal{P}/P_0$ and (*c*) efficiency η on the Reynolds number, Re. The simulation results are for $\delta_t/L = 0.15$, $\delta_t/L = 0.25$, $\chi = 5$ and $\mathcal{A}_\mathcal{R} = 2$.

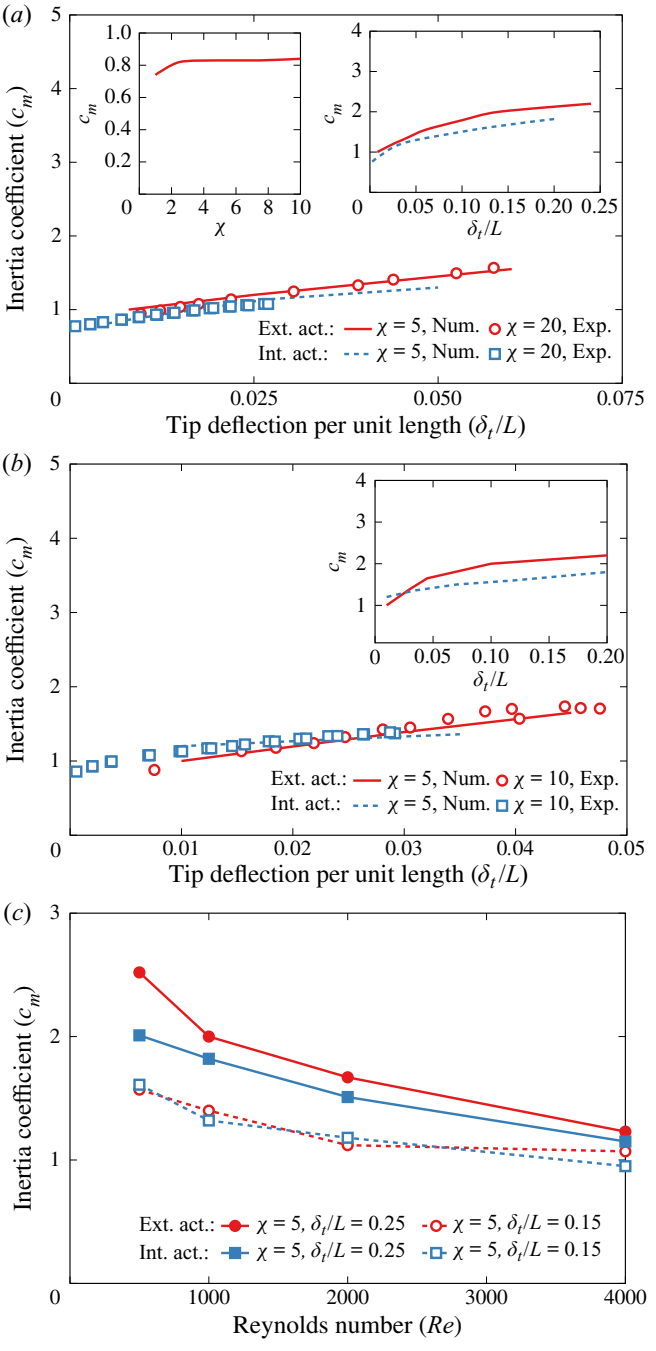

FIGURE 14. Dependence of inertia mass coefficient on the tip deflection in the linear oscillation regime of internally and externally actuated plates for $Re = 1000$, $\chi = 5$ and aspect ratios (*a*) $\mathcal{A}_\mathcal{R} = 2$ and (*b*) $\mathcal{A}_\mathcal{R} = 4$. (*c*) Dependence of the inertia mass coefficient on Re for $\mathcal{A}_\mathcal{R} = 2$, $\chi = 5$, $\delta_t/L = 0.05$ and $\delta_t/L = 0.25$. The left-hand inset in (*a*) shows the dependence of the inertia coefficient on the mass ratio for $\delta_t/L = 0.01$. The right-hand inset in panel (*a*) and inset in panel (*b*) show the inertia coefficient for nonlinear range of plate oscillations. In panels (*a*,*b*) the lines represent simulation results while the symbols represent experimental data, whereas panel (*c*) is simulation results only.

more important, the hydrodynamic efficiency is more sensitive to the difference in bending patterns of the internally and externally actuated plates. Conversely, at higher Reynolds number, the hydrodynamic efficiency converges to a constant value. This behaviour is consistent with the potential flow solution predicting that the efficiency is set by the tip kinematics.

In figures 14(*a*) and 14(*b*), we show the inertia coefficient c_m for plates with, respectively, $\mathcal{A}_\mathcal{R} = 2$ and $\mathcal{A}_\mathcal{R} = 4$ as a function of the tip deflection δ_t. We find close agreement between the experiments and simulations despite that they use different values of the mass ratio χ. As shown in the inset in figure 14(*a*), the inertia coefficient is nearly independent of χ for $\chi > 2.5$. This explains good agreement between simulations and experiments in figures 14(*a*) and 14(*b*), where the simulations are performed with $\chi = 5$, whereas the experimental plates are, respectively, characterized by $\chi = 20$ and $\chi = 10$.

Our experiments are limited to relatively small tip deflections, approximately $\delta_t = 0.05$. In the simulations, we explore a significantly wider range of δ_t, shown in the insets in figures 14(*a*) and 14(*b*). We find that the inertia coefficient plateaus with the increasing tip deflection, consistent for both types of actuation. Although it can be expected that the inertia coefficient is a sole function of the aspect ratio and the tip amplitude, our results show that the actuation method strongly affects c_m. Not only does c_m increase with the tip amplitude, but also the difference between c_m for two actuation methods increases with δ_t. For larger δ_t, the inertia coefficient for the externally actuated plate systematically exceeds c_m of the internally actuated plate. This result is in agreement with the hydrodynamic loading acting on the plate shown in figure 12. The externally actuated plate produces greater hydrodynamic forces and, therefore, is characterized by a higher inertia coefficient than the internally actuated plate.

In figure 14(*c*), we show simulation results for the inertia coefficient as a function of *Re*. The simulations are performed for externally and internally actuated plates with two values of the tip deflection. We find that c_m gradually decreases with *Re*. This result agrees with the theory (Van Eysden & Sader 2006, 2007; Tuck 1969) suggesting that as the viscous effects lessen and inertia dominates the inertia coefficient asymptotically converges to 1. Thus, at sufficiently high *Re* the added mass effect saturates and is nearly independent of the actuation method.

6. Conclusion

We systematically investigate and compare the hydrodynamics of elastic plates oscillating in an incompressible Newtonian fluid subjected to two distinct actuation methods. We probe the resonance oscillations in linear and nonlinear regimes of an externally actuated plate and a plate with an internal actuation. We pinpoint the critical differences in their bending patterns leading to different hydrodynamics performances. Specifically, the internally actuated plates display ‘cupping’ of the trailing edge due to a non-zero plate curvature induced by the internal bending moment. Furthermore, internally actuated plates exhibit a phase change of the plate angle along the plate length. Conversely, externally actuated plates have a zero curvature at the tip and an in-phase plate angle along the entire plate length. We show that this difference in bending pattern between internally and externally actuated plates leads to greater vorticity production by internally actuated plates and therefore enhances the viscous dissipation.

We find that for the same level of trailing edge displacement externally actuated plates outperform internally actuated plates in terms of the generated thrust and consumed power.

Furthermore, plates with external actuation are more efficient than plates with internal actuation with the exception of the smaller tip amplitudes, in which the efficiency of the externally actuated plates is limited due to the root displacement. For both actuation methods, we find that wider plates outperform more narrow plates due to the adverse effects of the side edge vortexes. Additionally, we also probe the effect of the actuation method on the plate inertia coefficient and find that the inertia coefficient is insensitive to the mass ratio for ratios greater than 2.5. In the linear oscillation regime, both actuation methods are characterized by similar values of the inertia coefficient. However, for larger tip deflections, the inertia coefficient of the externally actuated plate significantly exceeds that of internally actuated plates, which is related to the greater hydrodynamic forces experienced by the externally actuated plates. Thus we show that the inertia coefficient is not only a function of the aspect ratio and tip deflection, but also the actuation pattern.

We show that in the range $500 < Re < 4000$, the Reynolds number has minor influence on the thrust generated by the plate. We find that the plate kinematics defining the thrust production does not change significantly in this Re range. Conversely, Re impacts the power and, therefore, hydrodynamic efficiency of the plate. At lower Re, viscous effects increase the input power that, in turn, negatively affects the efficiency. Increasing Re also leads to a decrease of the inertia coefficient that converges to unity for higher Re. This behaviour is consistent with the analytical solution for an inviscid fluid. We find that these trends prevail for both actuation methods. Nevertheless, for lower Re the dependence of the plate hydrodynamics on the actuation method is more critical.

The results of our study provide useful guidelines for designing efficient biomimetic underwater robotic vehicles that utilize internally actuated propulsors such as piezoelectric actuators. Piezoelectric actuators are highly attractive due to a high degree of control over the bending pattern including a combined twisting–bending motion, large amplitude actuation, silent operation and the ease of interaction into robotic swimmers. Our study points to the need for improving the efficiency of internally actuated propulsors to match or exceed the efficiency achievable with externally actuated elastic fins. Different strategies can be explored to enhance the efficiency of piezoelectric propulsors including the use of passive attachments (Yeh & Alexeev 2016*a*), complex actuation cycles and a combination of an external and internal actuation. These studies are currently underway. Furthermore, the results of this work are useful for developing piezoelectric energy harvesting devices. In the latter scenario, fluid motion is harnessed to include oscillations of elastic structures with embedded piezoelectric transducers.

Acknowledgements

We thank the National Science Foundation (CBET-1705739) for financial support. The work used the Extreme Science and Engineering Discovery Environment (XSEDE) provided through Award TG-DMR180038.

Declaration of interests

The authors report no conflict of interest.

Supplementary material and movies

Supplementary material and movies are available at https://doi.org/10.1017/jfm.2020.915.

Appendix A. Inertia coefficient

We can rewrite (2.2) with an additional mass per area $\mathcal{M}$ as

$$\omega_{1,f} = \frac{\lambda_1^2}{L^2}\sqrt{\frac{D}{\sigma_s + \mathcal{M}}}. \tag{A 1}$$

By comparing the two definitions, we can obtain

$$\frac{\omega_{1,vac}^2}{\omega_{1,f}^2} = 1 + \frac{\mathcal{M}}{\sigma_s}. \tag{A 2}$$

For plates with moderate and high aspect ratios, the added mass can be expressed as $\mathcal{M} = (\pi/4)\rho W c_m = (\pi/4)\chi\sigma_s c_m$, with c_m being the inertia coefficient. We therefore evaluate the inertia coefficient as follows:

$$c_m = \frac{4}{\pi\chi}\left(\frac{\omega_{1,vac}^2}{\omega_{1,\mathrm{f}}^2} - 1\right). \tag{A 3}$$

Appendix B. Discretization

In discretized form (with $\gamma = 0$), (3.9) yields

$$\begin{aligned}
&\frac{\rho h}{\Delta t^2}\left(w_{i,j}^{n+1} - 2w_{i,j}^{n} + w_{i,j}^{n-1}\right) \\
&\quad = q_{i,j}^{n} + w_{i+2,j}^{n}\left(\frac{-D}{\Delta x^4}\right) + w_{i-2,j}^{n}\left(\frac{-D}{\Delta x^4}\right) + w_{i,j+2}^{n}\left(\frac{-D}{\Delta y^4}\right) + w_{i,j-2}^{n}\left(\frac{-D}{\Delta y^4}\right) \\
&\qquad + w_{i+1,j+1}^{n}\left(-\frac{2D}{\Delta x^2\Delta y^2} + \frac{N_{xyi,j}^{n}}{4\Delta x\Delta y}\right) + w_{i-1,j+1}^{n}\left(-\frac{2D}{\Delta x^2\Delta y^2} - \frac{N_{xyi,j}^{n}}{4\Delta x\Delta y}\right) \\
&\qquad + w_{i+1,j-1}^{n}\left(-\frac{2D}{\Delta x^2\Delta y^2} - \frac{N_{xyi,j}^{n}}{4\Delta x\Delta y}\right) + w_{i-1,j-1}^{n}\left(-\frac{2D}{\Delta x^2\Delta y^2} + \frac{N_{xyi,j}^{n}}{4\Delta x\Delta y}\right) \\
&\qquad + w_{i,j}^{n}\left[-D\left(\frac{6}{\Delta x^4} + \frac{8}{\Delta x^2\Delta y^2} + \frac{6}{\Delta y^4}\right) - \frac{2N_{xi,j}^{n}}{\Delta x^2} - \frac{2N_{yi,j}^{n}}{\Delta y^2}\right] \\
&\qquad + w_{i+1,j}^{n}\left[4D\left(\frac{1}{\Delta x^4} + \frac{1}{\Delta x^2\Delta y^2}\right) + \frac{N_{xi,j}^{n}}{\Delta x^2}\right] \\
&\qquad + w_{i-1,j}^{n}\left[4D\left(\frac{1}{\Delta x^4} + \frac{1}{\Delta x^2\Delta y^2}\right) + \frac{N_{xi,j}^{n}}{\Delta x^2}\right] \\
&\qquad + w_{i,j+1}^{n}\left[4D\left(\frac{1}{\Delta y^4} + \frac{1}{\Delta x^2\Delta y^2}\right) + \frac{N_{yi,j}^{n}}{\Delta y^2}\right] \\
&\qquad + w_{i,j-1}^{n}\left[4D\left(\frac{1}{\Delta y^4} + \frac{1}{\Delta x^2\Delta y^2}\right) + \frac{N_{yi,j}^{n}}{\Delta y^2}\right].
\end{aligned} \tag{B 1}$$

To constrain plate stretching during the deformation we impose the inextensibility condition. This condition is enforced numerically by introducing a differential arclength

$\mathrm{d}s^2 = \mathrm{d}x^2 + \mathrm{d}w^2$ that is numerically approximated as

$$x_{i+1} = x_i + \sqrt{\Delta s^2 - (w_{i+1} - w_i)^2}. \tag{B 2}$$

REFERENCES

ALBEN, S. 2009 On the swimming of a flexible body in a vortex street. *J. Fluid Mech.* **635**, 27–45.

ALBEN, S., WITT, C., BAKER, T. V., ANDERSON, E. & LAUDER, G. V. 2012 Dynamics of freely swimming flexible foils. *Phys. Fluids* **24** (5), 051901.

ALEXEEV, A. & BALAZS, A. C. 2007 Designing smart systems to selectively entrap and burst microcapsules. *Soft Matt.* **3** (12), 1500–1505.

ALEXEEV, A., VERBERG, R. & BALAZS, A. C. 2005 Modeling the motion of microcapsules on compliant polymeric surfaces. *Macromolecules* **38** (24), 10244–10260.

ALEXEEV, A., VERBERG, R. & BALAZS, A. C. 2006 Modeling the interactions between deformable capsules rolling on a compliant surface. *Soft Matt.* **2** (6), 499–509.

AMABILI, M. & PAIDOUSSIS, M. P. 2003 Review of studies on geometrically nonlinear vibrations and dynamics of circular cylindrical shells and panels, with and without fluid-structure interaction. *Appl. Mech. Rev.* **56** (4), 349–381.

ANDERSON, E. J., MCGILLIS, W. R. & GROSENBAUGH, M. A. 2001 The boundary layer of swimming fish. *J. Expl Biol.* **204** (1), 81–102.

ANDERSON, J. M., STREITLIEN, K., BARRETT, D. S. & TRIANTAFYLLOU, M. S. 1998 Oscillating foils of high propulsive efficiency. *J. Fluid Mech.* **360**, 41–72.

AURELI, M., BASARAN, M. E. & PORFIRI, M. 2012 Nonlinear finite amplitude vibrations of sharp-edged beams in viscous fluids. *J. Sound Vib.* **331** (7), 1624–1654.

BHALLA, A. P. S., BALE, R., GRIFFITH, B. E. & PATANKAR, N. A. 2013 A unified mathematical framework and an adaptive numerical method for fluid–structure interaction with rigid, deforming, and elastic bodies. *J. Comput. Phys.* **250**, 446–476.

BIDKAR, R. A., KIMBER, M., RAMAN, A., BAJAJ, A. K. & GARIMELLA, S. V. 2009 Nonlinear aerodynamic damping of sharp-edged flexible beams oscillating at low Keulegan–Carpenter numbers. *J. Fluid Mech.* **634**, 269–289.

BORAZJANI, I. & SOTIROPOULOS, F. 2008 Numerical investigation of the hydrodynamics of carangiform swimming in the transitional and inertial flow regimes. *J. Expl Biol.* **211** (10), 1541–1558.

BOUZIDI, M., FIRDAOUSS, M. & LALLEMAND, P. 2001 Momentum transfer of a Boltzmann-lattice fluid with boundaries. *Phys. Fluids* **13** (11), 3452–3459.

BRANSCOMB, J. & ALEXEEV, A. 2010 Designing ciliated surfaces that regulate deposition of solid particles. *Soft Matt.* **6** (17), 4066–4069.

CEN, L. & ERTURK, A. 2013 Bio-inspired aquatic robotics by untethered piezohydroelastic actuation. *Bioinspir. Biomim.* **8** (1), 016006.

CHA, Y., KIM, H. & PORFIRI, M. 2013 Energy harvesting from underwater base excitation of a piezoelectric composite beam. *Smart Mater. Struct.* **22** (11), 115026.

CHEN, X.-J., WU, Y.-S., CUI, W.-C. & JENSEN, J. J. 2006 Review of hydroelasticity theories for global response of marine structures. *Ocean Engng* **33** (3–4), 439–457.

CHEN, Z., SHATARA, S. & TAN, X. 2009 Modeling of biomimetic robotic fish propelled by an ionic polymer–metal composite caudal fin. *IEEE ASME Trans. Mechatron.* **15** (3), 448–459.

CHEN, Z., UM, T. I., ZHU, J. & BART-SMITH, H. 2011 Bio-inspired robotic cownose ray propelled by electroactive polymer pectoral fin. In *ASME 2011 International Mechanical Engineering Congress and Exposition*, pp. 817–824. American Society of Mechanical Engineers Digital Collection.

CHUN, B. & LADD, A. J. C. 2007 Interpolated boundary condition for lattice Boltzmann simulations of flows in narrow gaps. *Phys. Rev.* E **75**, 066705.

COMBES, S. A. & DANIEL, T. L. 2001 Shape, flapping and flexion: wing and fin design for forward flight. *J. Expl Biol.* **204** (12), 2073–2085.

DAI, H., LUO, H., DE SOUSA, P. J. S. A. F. & DOYLE, J. F. 2012 Thrust performance of a flexible low-aspect-ratio pitching plate. *Phys. Fluids* **24** (10), 101903.

De Rosis, A. & Lévêque, E. 2016 Central-moment lattice Boltzmann schemes with fixed and moving immersed boundaries. *Comput. Maths Applics.* **72** (6), 1616–1628.

Dowell, E. H. & Hall, K. C. 2001 Modeling of fluid-structure interaction. *Annu. Rev. Fluid Mech.* **33** (1), 445–490.

Elmer, F.-J. & Dreier, M. 1997 Eigenfrequencies of a rectangular atomic force microscope cantilever in a medium. *J. Appl. Phys.* **81** (12), 7709–7714.

Eloy, C. & Schouveiler, L. 2011 Optimisation of two-dimensional undulatory swimming at high reynolds number. *Intl J. Non-Linear Mech.* **46** (4), 568–576.

Engels, T., Kolomenskiy, D., Schneider, K. & Sesterhenn, J. 2017 Numerical simulation of vortex-induced drag of elastic swimmer models. *Theor. Appl. Mech. Lett.* **7** (5), 280–285.

Erturk, A. & Delporte, G. 2011 Underwater thrust and power generation using flexible piezoelectric composites: an experimental investigation toward self-powered swimmer-sensor platforms. *Smart Mater. Struct.* **20** (12), 125013.

Erturk, A. & Inman, D. J. 2011 *Piezoelectric Energy Harvesting*. John Wiley & Sons.

Esposito, C. J., Tangorra, J. L., Flammang, B. E. & Lauder, G. V. 2012 A robotic fish caudal fin: effects of stiffness and motor program on locomotor performance. *J. Expl Biol.* **215** (1), 56–67.

Facci, A. L. & Porfiri, M. 2013 Analysis of three-dimensional effects in oscillating cantilevers immersed in viscous fluids. *J. Fluids Struct.* **38**, 205–222.

Fish, F. & Lauder, G. V. 2006 Passive and active flow control by swimming fishes and mammals. *Annu. Rev. Fluid Mech.* **38**, 193–224.

Flammang, B. E. & Lauder, G. V. 2009 Caudal fin shape modulation and control during acceleration, braking and backing maneuvers in bluegill sunfish, lepomis macrochirus. *J. Expl Biol.* **212** (2), 277–286.

Ghatkesar, M. K., Braun, T., Barwich, V., Ramseyer, J.-P., Gerber, C., Hegner, M. & Lang, H. P. 2008 Resonating modes of vibrating microcantilevers in liquid. *Appl. Phys. Lett.* **92** (4), 043106.

Hoover, A. P., Cortez, R., Tytell, E. D. & Fauci, L. J. 2018 Swimming performance, resonance and shape evolution in heaving flexible panels. *J. Fluid Mech.* **847**, 386–416.

Hou, G., Wang, J. & Layton, A. 2012 Numerical methods for fluid-structure interaction – a review. *Commun. Comput. Phys.* **12** (2), 337–377.

Hu, H., Liu, J., Dukes, I. & Francis, G. 2006 Design of 3d swim patterns for autonomous robotic fish. In *2006 IEEE/RSJ International Conference on Intelligent Robots and Systems*, pp. 2406–2411. IEEE.

Jayne, B. C. & Lauder, G. V. 1995 Speed effects on midline kinematics during steady undulatory swimming of largemouth bass, micropterus salmoides. *J. Expl Biol.* **198** (2), 585–602.

Keulegan, G. H. 1958 Forces on cylinders and plates in an oscillating fluid. *J. Res. Natl Bur. Stand.* **2857**, 423–440.

Kirchhoff, G. 1850 Über das Gleichgewicht und die Bewegung einer elastischen Scheibe. *J. Reine Angew. Math.* **1850** (40), 51–88.

Kolomenskiy, D., Moffatt, H. K., Farge, M. & Schneider, K. 2011 The Lighthill–Weis-Fogh clap–fling–sweep mechanism revisited. *J. Fluid Mech.* **676**, 572–606.

Kopman, V., Laut, J., Acquaviva, F., Rizzo, A. & Porfiri, M. 2015 Dynamic modeling of a robotic fish propelled by a compliant tail. *IEEE J. Ocean. Engng* **40** (1), 209–221.

Ladd, A. J. C. & Verberg, R. 2001 Lattice-Boltzmann simulations of particle-fluid suspensions. *J. Stat. Phys.* **104** (5–6), 1191–1251.

Lauder, G. V. & Tangorra, J. L. 2015 *Fish Locomotion: Biology and Robotics of Body and Fin-Based Movements*, pp. 25–49. Springer.

Lauder, G. V. & Tytell, E. D. 2005 Hydrodynamics of undulatory propulsion. *Fish Physiol.* **23**, 425–468.

Li, G., Müller, U. K., van Leeuwen, J. L. & Liu, H. 2014 Escape trajectories are deflected when fish larvae intercept their own C-start wake. *J. R. Soc. Interface* **11** (101), 20140848.

Lighthill, M. J. 1960 Note on the swimming of slender fish. *J. Fluid Mech.* **9** (2), 305–317.

Lighthill, M. J. 1970 Aquatic animal propulsion of high hydromechanical efficiency. *J. Fluid Mech.* **44** (2), 265–301.

LIGHTHILL, M. J. 1971 Large-amplitude elongated-body theory of fish locomotion. *Proc. R. Soc. Lond.* B **179** (1055), 125–138.

LIU, G., REN, Y., DONG, H., AKANYETI, O., LIAO, J. C. & LAUDER, G. V. 2017 Computational analysis of vortex dynamics and performance enhancement due to body–fin and fin–fin interactions in fish-like locomotion. *J. Fluid Mech.* **829**, 65–88.

LIU, H. & AONO, H. 2009 Size effects on insect hovering aerodynamics: an integrated computational study. *Bioinspir. Biomim.* **4** (1), 015002.

MAO, W. & ALEXEEV, A. 2014 Motion of spheroid particles in shear flow with inertia. *J. Fluid Mech.* **749**, 145–166.

MASOUD, H. & ALEXEEV, A. 2010 Resonance of flexible flapping wings at low Reynolds number. *Phys. Rev.* E **81**, 056304.

MASOUD, H. & ALEXEEV, A. 2011 Harnessing synthetic cilia to regulate motion of microparticles. *Soft Matt.* **7** (19), 8702–8708.

MASOUD, H., BINGHAM, B. I. & ALEXEEV, A. 2012 Designing maneuverable micro-swimmers actuated by responsive gel. *Soft Matt.* **8** (34), 8944–8951.

MCHENRY, M. J., PELL, C. A. & LONG, J. H. 1995 Mechanical control of swimming speed: stiffness and axial wave form in undulating fish models. *J. Expl Biol.* **198** (11), 2293–2305.

MICHELIN, S. & LLEWELLYN SMITH, S. G. 2009 Resonance and propulsion performance of a heaving flexible wing. *Phys. Fluids* **21** (7), 071902.

MITTAL, R., DONG, H., BOZKURTTAS, M., NAJJAR, F. M., VARGAS, A. & VON LOEBBECKE, A. 2008 A versatile sharp interface immersed boundary method for incompressible flows with complex boundaries. *J. Comput. Phys.* **227** (10), 4825–4852.

MORISON, J. R., JOHNSON, J. W. & SCHAAF, S. A. 1950 The force exerted by surface waves on piles. *J. Petrol. Technol.* **2** (5), 149–154.

NAUEN, J. C. & LAUDER, G. V. 2002 Hydrodynamics of caudal fin locomotion by chub mackerel, Scomber japonicus (scombridae). *J. Expl Biol.* **205** (12), 1709–1724.

PARAZ, F., SCHOUVEILER, L. & ELOY, C. 2016 Thrust generation by a heaving flexible foil: resonance, nonlinearities, and optimality. *Phys. Fluids* **28** (1), 011903.

PHILEN, M. & NEU, W. 2011 Hydrodynamic analysis, performance assessment, and actuator design of a flexible tail propulsor in an artificial alligator. *Smart Mater. Struct.* **20** (9), 094015.

QUINN, D. B., LAUDER, G. V. & SMITS, A. J. 2014 Scaling the propulsive performance of heaving flexible panels. *J. Fluid Mech.* **738**, 250–267.

RASPA, V., RAMANANARIVO, S., THIRIA, B. & GODOY-DIANA, R. 2014 Vortex-induced drag and the role of aspect ratio in undulatory swimmers. *Phys. Fluids* **26** (4), 041701.

SADER, J. E. 1998 Frequency response of cantilever beams immersed in viscous fluids with applications to the atomic force microscope. *J. Appl. Phys.* **84** (1), 64–76.

SADER, J. E., COSSÉ, J., KIM, D., FAN, B. & GHARIB, M. 2016 Large-amplitude flapping of an inverted flag in a uniform steady flow–a vortex-induced vibration. *J. Fluid Mech.* **793**, 524–555.

SARPKAYA, T. 1976 Vortex shedding and resistance in harmonic flow about smooth and rough circular cylinders at high Reynolds numbers. *Tech. Rep.* NPS-59SL76021. Naval Postgraduate School, Monterey, CA.

SARPKAYA, T. 1986 Force on a circular cylinder in viscous oscillatory flow at low Keulegan–Carpenter numbers. *J. Fluid Mech.* **165**, 61–71.

SARPKAYA, T. & ISAACSON, M. 1981 *Mechanics of Waves Forces on Offshore Structures*. Van Nostrand.

SCARADOZZI, D., PALMIERI, G., COSTA, D. & PINELLI, A. 2017 BCF swimming locomotion for autonomous underwater robots: a review and a novel solution to improve control and efficiency. *Ocean Engng* **130**, 437–453.

SFAKIOTAKIS, M., LANE, D. M. & DAVIES, J. B. C. 1999 Review of fish swimming modes for aquatic locomotion. *IEEE J. Ocean. Engng* **24** (2), 237–252.

SHAHAB, S., TAN, D. & ERTURK, A. 2015 Hydrodynamic thrust generation and power consumption investigations for piezoelectric fins with different aspect ratios. *Eur. Phys. J. Spec. Top.* **224** (17–18), 3419–3434.

SHELLEY, M. J. & ZHANG, J. 2011 Flapping and bending bodies interacting with fluid flows. *Annu. Rev. Fluid Mech.* **43**, 449–465.

SU, Z., YU, J., TAN, M. & ZHANG, J. 2014 Implementing flexible and fast turning maneuvers of a multijoint robotic fish. *IEEE ASME Trans. Mechatron.* **19** (1), 329–338.

TAN, D. & ERTURK, A. 2018 On the coupling of nonlinear macro-fiber composite piezoelectric cantilever dynamics with hydrodynamic loads. In *Active and Passive Smart Structures and Integrated Systems XII*, vol. 10595, p. 105950R. International Society for Optics and Photonics.

TIMOSHENKO, S. & WOINOWSKY-KRIEGER, S. 1959 *Theory of Plates and Shells*. McGraw-Hill.

TRIANTAFYLLOU, M. S. & TRIANTAFYLLOU, G. S. 1995 An efficient swimming machine. *Sci. Am.* **272** (3), 64–70.

TUCK, E. O. 1969 Calculation of unsteady flows due to small motions of cylinders in a viscous fluid. *J. Engng Maths* **3** (1), 29–44.

VAN EYSDEN, C. A. & SADER, J. E. 2006 Resonant frequencies of a rectangular cantilever beam immersed in a fluid. *J. Appl. Phys.* **100** (11), 114916.

VAN EYSDEN, C. A. & SADER, J. E. 2007 Frequency response of cantilever beams immersed in viscous fluids with applications to the atomic force microscope: arbitrary mode order. *J. Appl. Phys.* **101** (4), 044908.

WEAVER, W. JR., TIMOSHENKO, S. P. & YOUNG, D. H. 1990 *Vibration Problems in Engineering*. John Wiley & Sons.

WEISS, J. 1991 The dynamics of enstrophy transfer in two-dimensional hydrodynamics. *Physica* D **48** (2–3), 273–294.

WU, T. Y.-T. 1961 Swimming of a waving plate. *J. Fluid Mech.* **10** (3), 321–344.

YEH, P. D. & ALEXEEV, A. 2014 Free swimming of an elastic plate plunging at low Reynolds number. *Phys. Fluids* **26** (5), 053604.

YEH, P. D. & ALEXEEV, A. 2016*a* Biomimetic flexible plate actuators are faster and more efficient with a passive attachment. *Acta Mechanica Sin.* **32** (6), 1001–1011.

YEH, P. D. & ALEXEEV, A. 2016*b* Effect of aspect ratio in free-swimming plunging flexible plates. *Comput. Fluids* **124**, 220–225.

YEH, P. D., LI, Y. & ALEXEEV, A. 2017 Efficient swimming using flexible fins with tapered thickness. *Phys. Rev. Fluids* **2**, 102101.

YU, C.-L., TING, S.-C., YEH, M.-K. & YANG, J.-T. 2011 Three-dimensional numerical simulation of hydrodynamic interactions between pectoral-fin vortices and body undulation in a swimming fish. *Phys. Fluids* **23** (9), 091901.

ZHANG, J., LIU, N.-S. & LU, X.-Y. 2010 Locomotion of a passively flapping flat plate. *J. Fluid Mech.* **659**, 43–68.

ZHU, Q., WOLFGANG, M. J., YUE, D. K. P. & TRIANTAFYLLOU, M. S. 2002 Three-dimensional flow structures and vorticity control in fish-like swimming. *J. Fluid Mech.* **468**, 1–28.